Key Points:
- Stereo ENA imaging has revealed new dimensionality and structure of ring current ions; LAE analysis has revealed causal connections
- Ion temperature, ion composition, and neutral exospheric H density have been imaged for events spanning solar cycles 23 and 24
- Global models have been measurably improved, and multimission observations have enriched the study of the cross-scale geospace response

Correspondence to:
J. Goldstein,
jgoldstein@swri.edu

The Big Picture: Imaging of the Global Geospace Environment by the TWINS Mission

J. Goldstein[1,2] (ID) **and D. J. McComas[3]** (ID)

[1]Space Science Department, Southwest Research Institute, San Antonio, TX, USA, [2]Department of Physics and Astronomy, University of Texas at San Antonio, San Antonio, TX, USA, [3]Department of Astrophysical Sciences, Princeton University, Princeton, NJ, USA

Abstract Encircling our planet at distances of 2.5 to 8 Earth radii is a dynamic plasma population known as the ring current (RC). During geomagnetic storms, the solar wind's interaction with Earth's magnetic field pumps petaJoules of energy into the RC, energizing and transporting particles. To measure the global geospace response, RC imaging is performed by capturing energetic neutral atoms (ENAs) created by charge exchange between geospace ions and the neutral exosphere. The H exosphere is itself imaged via its geocoronal Lyman-α glow. Two Wide-angle Imaging Neutral-atom Spectrometers (TWINS) is a stereoscopic ENA and Lyman-α imaging mission that has recorded the deep minimum of solar cycle (SC) 23 and the moderate maximum of SC 24, observing geospace conditions ranging from utterly quiet to major storms. This review covers TWINS studies of the geospace response published during 2013 to 2017. Stereo ENA imaging has revealed new dimensionality and structure of RC ions. Continuous coverage by two imagers has allowed monitoring storms from start to finish. Deconvolution of the low-altitude signal has extended ENA analysis and revealed causal connections between the trapped and precipitating ion populations. ENA-based temperature and composition analyses have been refined, validated, and applied to an unprecedented sequence of solar activity changes in SC 23 and SC 24. Geocoronal imaging has revealed a surprising amount of time variability and structure in the neutral H exosphere, driven by both Sun and solar wind. Global models have been measurably improved. Routine availability of simultaneous in situ measurements has fostered huge leaps forward in the areas of ENA validation and cross-scale studies.

Plain Language Summary This paper is a review of the last several years of science results from the National Aeronautics and Space Administration (NASA) Two Wide-angle Imaging Neutral-atom Spectrometers (TWINS) mission, which performs imaging of the near-Earth space environment, known as geospace. TWINS geospace imaging has revealed new structure and behavior in the ionized and neutral gases surrounding the Earth during geomagnetic storms—disturbances in the plasmas and fields caused by changes in the solar wind.

1. Introduction: Imaging the Global Dynamics of the Geospace Environment

The geospace environment is a dynamic region occupied by a variety of plasmas and neutral gases. The former group includes the different plasmas of the magnetosphere and ionosphere (Chapman, 1931; Gold, 1959; Yonezawa, 1966). The latter group is composed mainly of neutral hydrogen and oxygen in the exosphere (Singer, 1960). These populations respond separately to energy input from the Sun and solar wind. They also interact with each other, producing feedback effects that can modify or even overcome the external forcing (Borovsky, 2014; Goldstein, 2006; Lotko, 2013). Global imaging of the geospace region provides a system-level, "big-picture" view of the response of this system of coupled plasmas and gases. This review paper focuses on recent results from the National Aeronautics and Space Administration (NASA) Two Wide-angle Imaging Neutral-atom Spectrometers (TWINS) geospace imaging mission.

1.1. The Ring Current and Neutral Exosphere
1.1.1. Geomagnetic Storms
Geomagnetic storms are disturbances in the plasmas and fields of the geospace environment, caused by the ever changing conditions in the solar wind. During storms, the solar wind's plasma and embedded interplanetary magnetic field (IMF) strike the Earth's magnetic field, transferring energy into the magnetosphere.

Elevated solar wind plasma pressure compresses the magnetosphere (Dessler & Parker, 1959). Southward IMF (i.e., pointed opposite to the Earth's field) initiates dayside magnetopause reconnection, driving a global convection cycle inside the magnetosphere (Dungey, 1961).

The frequency and strength of geomagnetic storms vary with the phase of the 11 year solar cycle. During solar maximum, storms are most commonly triggered by coronal mass ejections or CMEs (Borovsky & Denton, 2006; Cane & Richardson, 2003; Gosling, 1993; Gosling et al., 1974; Webb & Howard, 1994). In a CME event, solar plasma (up to 10^{13} kg) and magnetic flux are ejected into interplanetary space. Fast CMEs drive shocks in the solar wind, which compress the magnetosphere and are a major source of solar energetic particles that can damage satellites and harm astronauts. CME-driven storms tend to be strong.

A second type of solar wind driver is the corotating interaction region (CIR) and its associated high-speed stream (HSS) that emerges from a weak-field coronal hole on the Sun's surface (Burlaga, 1975; Dryer et al., 1978; Fisk & Lee, 1980). CIRs and HSSs are more prevalent during the declining phase of the solar cycle, when coronal holes are longer lived. The intense CIR magnetic field forms a spiral as it propagates radially through interplanetary space and therefore tends to trigger geomagnetic storms that recur with a periodicity of about 27 days, i.e., the solar synodic rotation period (Borovsky & Denton, 2006; Tsurutani et al., 1995, 2006). CIR-driven storms are generally weaker than those triggered by CMEs.

1.1.2. Ring Current

A major effect of geomagnetic storms is intensification of the Earth's ring current. The ring current (RC) is a population of hot (a few keV to hundreds of keV) ions (mostly H^+, O^+) and electrons that encircle the Earth at geocentric distances of 16,000 km to 51,000 km, or 2.5 to 8 Earth radii (R_E); cf. Figure 1a. During geomagnetic storms, the interaction of the solar wind with the Earth's magnetic field can pump petaJoules (10^{15} J) of energy into the ring current (Dessler & Parker, 1959; Sckopke, 1966). In addition to energizing and transporting RC particles, this enormous energy also may trigger space weather events affecting satellites, communications, power grids, or humans in space (Bothmer & Daglis, 2007).

The ring current's response to solar wind driving is one of the defining characteristics of geomagnetic storms. The commonly used Dst (disturbance storm time) and SymH (symmetric H-component) storm indices (Sugiura & Kamei, 1991; Wanliss & Showalter, 2006) measure the strength of a storm as a RC-induced deflection of the magnetic field at the Earth's surface—ranging from a few tens of nanoteslas (for weak storms) to hundreds of nanoteslas (major storms). The ring current energy density is dominated by ions trapped in the geomagnetic field. During storms and substorms magnetotail plasma is injected into the inner magnetosphere to form an asymmetric torus, known as the partial ring current (Figure 2a). During storm recovery or quiet times, azimuthal magnetic drifts tend to disperse the distribution into a more symmetric torus.

Because of the ring current's central role in geomagnetic storms, understanding the dynamics of keV-charged particles is important. Within the RC torus, ions move along the magnetic field (**B**) on helical paths, as shown in Figure 1b. The angle between the ion helix and the B field is called pitch angle. The ion pitch angle at the magnetic equator determines how far away from the equator (i.e., toward the ionosphere) the ion will magnetically mirror. Particles with large pitch angles (near 90°) are trapped close to the equator. Particles with smaller pitch angles spiral farther along the field. Particles whose pitch angles carry them to lower-altitude mirror points—into the so-called loss cone—are precipitated (lost) into the ionosphere (Figure 1a). Injected particles with an isotropic pitch angle distribution (PAD) can spill over into the loss cone and precipitate. Subsequent to injection, Coulomb collisions and wave-particle interactions can cause pitch-angle scattering into the loss cone (Fok et al., 1991; Gary et al., 1995). Particle precipitation is a significant, observable loss mechanism for the RC and can help govern the duration of storms.

The ring current response can be complex. For example, the strongest geomagnetic storms often contain two distinct dips in Dst, so-called double-dip storms (Akasofu et al., 1963; Kamide et al., 1998). In double-dip storms, successive intensifications of the ring current occur, with the second increase commencing before the first one completely recovers. This two-step process involves an interplay between solar wind driving and ring current that is only partially understood; suggestions have included multiple successive southward IMF intervals (Tsurutani et al., 1988), two spatially distinct current rings (Akasofu et al., 1963), and two epochs of different ion composition (Yokoyama & Kamide, 1997).

1.1.3. Neutral Exosphere

A second geospace population plays a major role in ring current dynamics: the neutral exosphere (Figure 2b). Bound to the Earth by gravity, the neutral gas density falls off roughly exponentially with radius. The scale
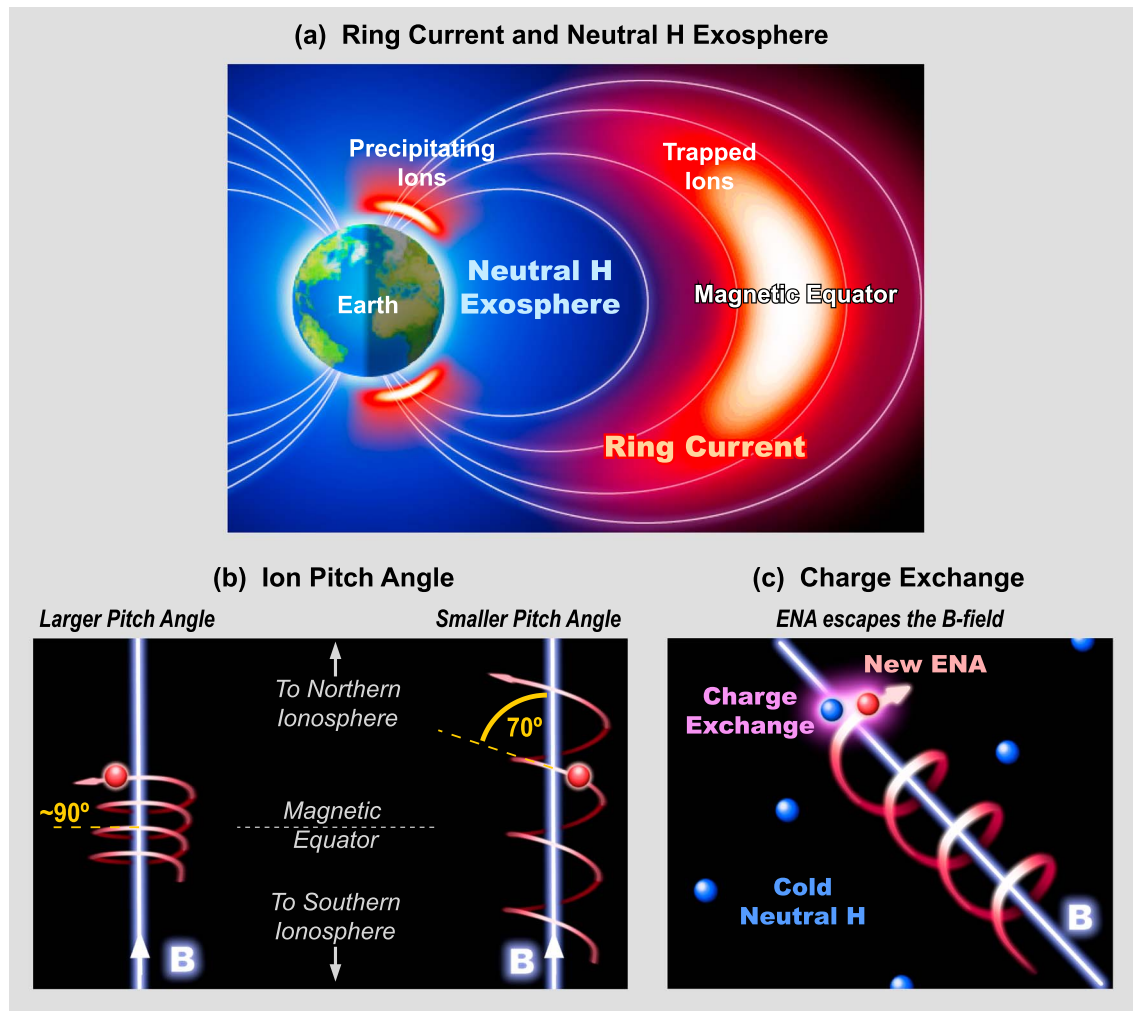
Figure 1. Two major geospace populations and how they interact. (a) Schematic view of the ring current and exosphere. The ring current is composed of hot (keV) ions and electrons bound to the Earth's magnetic field—both trapped near the magnetic equator and precipitating into the ionosphere. The neutral hydrogen (H) exosphere consists of cold (eV) atoms bound to the Earth by gravity. (b) Ions spiral along the magnetic field (*B*). Pitch angle (PA) is the angle between the ion helix and *B*. Ions with large PA (near 90°) are trapped very near the magnetic equator. Ions with smaller pitch angle spiral farther from the equator. Ions with sufficiently small pitch angles precipitate into the ionosphere. (c) Charge exchange is the main interaction between the ring current and neutral exosphere. In this process, a hot ion spiraling along the magnetic field obtains an electron from a nearby cold neutral atom. Thus neutralized, the newly created energetic neutral atom (ENA) escapes the magnetic field.

height of the exponential distribution is different for each atomic species. The neutral hydrogen distribution extends several R_E above the Earth, so that there is significant overlap with the ring current (Figure 1a). Heavier oxygen atoms have a much smaller-scale height, and thus extend only several hundred km in altitude (Anderson & Francis, 1966; Singer, 1960).

In the space occupied by trapped ring current ions (2.5 to 8 R_E), the neutral exosphere is almost entirely composed of H atoms. Charge exchange (Figure 1c) occurs in this overlap region, in which a hot ring current ion acquires an electron from a nearby cold neutral atom and is converted into an ENA (Stuart, 1959). No longer bound to the magnetic field, the newly created ENA escapes. Charge exchange has long been known to be a major cause of the decay of the ring current (Dessler & Parker, 1959; Daglis et al., 1999). At lower altitudes, mirroring ions can also undergo charge exchange with the dense oxygen exosphere, further accelerating the RC decay.

1.2. TWINS ENA and Lyman-α Geocoronal Imaging

Creation of ENAs by charge exchange is not only a loss process; it also enables remote sensing of the ring current, as first demonstrated using International Sun-Earth Explorer-1 data (Roelof, 1987) and many times
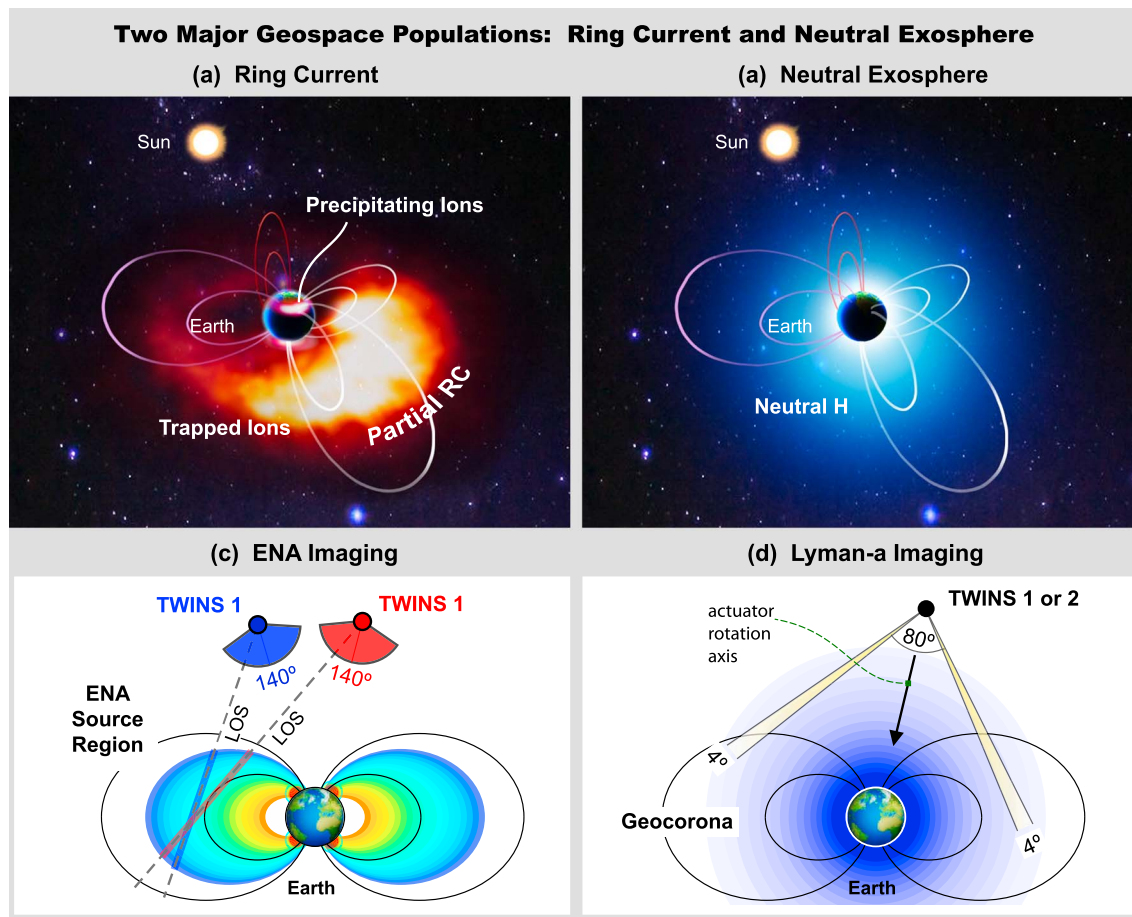
Figure 2. Two major geospace populations and how they are imaged. (a) The ions of the ring current are found at geocentric distances of 2.5 to 8 Earth radii (R_E). Geomagnetic storms pump energy into the ring current, forming an asymmetric, partial torus. (b) The neutral hydrogen (H) exosphere extends several R_E into space. Heavier oxygen (O) gas reaches only several hundred km altitude. (c) Energetic neutral atom (ENA) imaging consists of collecting energetic neutrals from the intersection of the line of sight (LOS) and the source region. TWINS gathers ENAs from LOS within a 140° × 360° viewing cone. (d) Lyman-α imaging measures the geocorona or glow from neutral H atoms. TWINS collects Lyman-α photons from an annular 4° × 360° FOV whose cone vertex angle is 80°.

in the decades since then (Goldstein & McComas, 2013), e.g., by the Imager for Magnetopause-to-Aurora Global Exploration (IMAGE) mission (Burch, 2003) whose results are cited several times in the rest of this review. ENA imaging obtains a macroscopic picture of the ring current, allowing us to study system-level changes and identify causal links.

Two Wide-angle Imaging Neutral-atom Spectrometers (TWINS) is the first stereo geospace imager mission (Goldstein & McComas, 2013; McComas, Allegrini, Baldonado, et al., 2009), launched as part of the NASA Small Explorer Mission of Opportunity program. Starting in 2008, TWINS began imaging from two spacecraft in widely separated Molniya orbits (cf. orbit plot of Figure 3c). The highly elliptical (7.2 R_E apogee) Molniya orbit is well suited to ring current imaging because of its high orbital inclination (63.4°) that does not precess. The primary instrument on TWINS is an ENA imager that captures energetic neutrals from 1 to 100 keV/u (where u is one atomic mass unit, 1.66×10^{-27} kg), with at least 4° × 4° angular resolution, at a 1 min cadence. Figure 3 shows stereo ENA images of the ring current during a major geomagnetic storm (peak Dst of −204 nT) on 23 June 2015. These two images were taken from two distinct vantage points. The TWINS 1 image was obtained from prenoon magnetic local time (MLT). The TWINS 2 image was obtained from near dusk MLT. The images were recorded several hours after the storm peak, under still very disturbed conditions (Dst of −161 nT). Each image has emissions from two sources. The ring current emission (RCE) is from the trapped ion distribution. The low-altitude emission (LAE) is from ions mirroring below ∼800 km altitude.
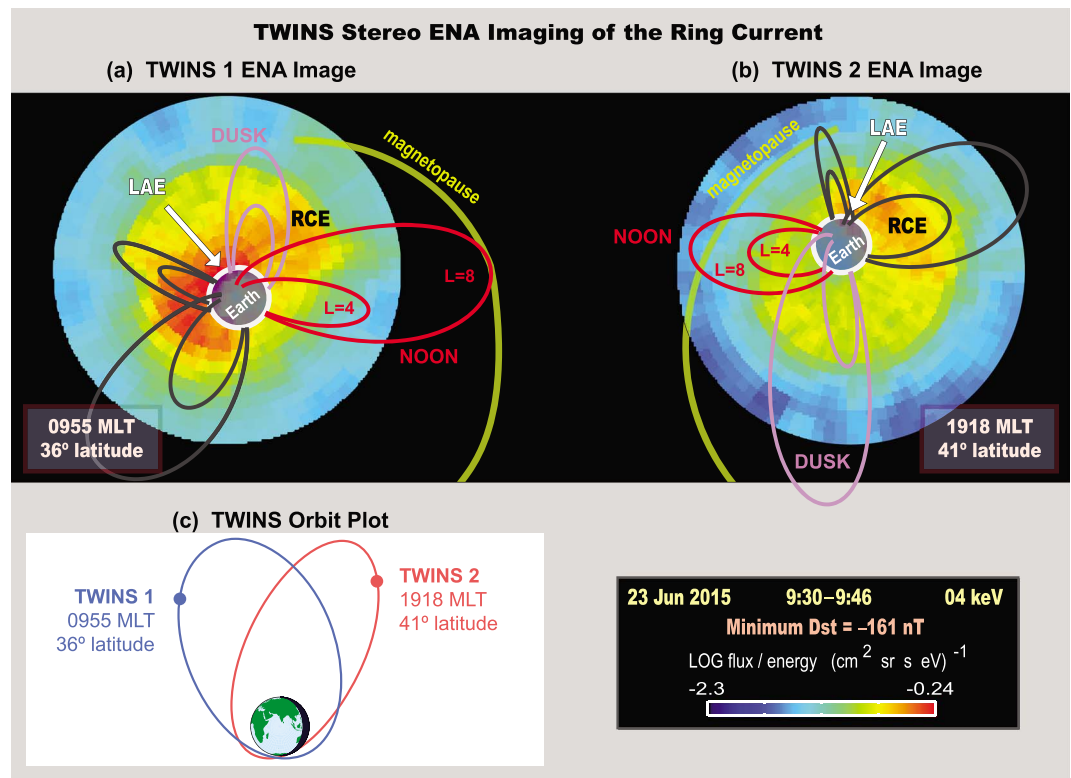
Figure 3. Storm time stereo energetic neutral atom (ENA) image. (a, b) Stereo ENA images by TWINS during a major storm (peak −204 nT) on 23 June 2015. Visible in each image are both low-altitude emissions (LAEs) from precipitating ions and high-altitude ring current emissions (RCE). The Earth's limb is drawn along with dipole magnetic field lines at four cardinal local times (noon, dusk, midnight, and dawn) and at two L values (4, 8). The model magnetopause (yellow) is from Shue et al. (1997). (c) TWINS Molniya orbits (Earth-centered inertial coordinates) and locations at the time of the images.

Complementing the ENA imager on each spacecraft is a Lyman-α imager to monitor the geocoronal glow of cold exospheric neutral H atoms. The Lyman-α detector (LAD) registers 121.6 nm light with a bandwidth of 10 nm (Nass et al., 2006). Geocoronal imaging is extremely useful to help deconvolve the global RC distribution from an ENA image (cf. section 1.2.1). Recent results also have shown unexpected dynamics of the neutral exosphere (section 2.5).

For thorough discussions of TWINS instrumentation and image-making techniques, see Bailey and Gruntman (2011), McComas, Allegrini, Baldonado, et al. (2009), McComas et al. (2012), and Valek et al. (2013).

1.2.1. ENA Imaging Technique

Figure 2c illustrates the TWINS ENA imaging technique. Each imager is composed of two sensors that together cover an instantaneous field of view (FOV) of 140° × 4°. These sensors are mounted on a rotating actuator that sweeps out an (approximately) Earth-nadir-centered viewing cone (140° × 360°) via a back-and-forth (windshield-wiper) motion. Within this FOV, each individual TWINS pixel collects ENAs from the intersection of the pixel line of sight (LOS) and the ENA source region. The intensity of the ENA ring current emission along each LOS is thus given by

$$J_{RCE} = \sigma_H \int_{LOS} n_H \, J_{ion} \, dS, \qquad (1)$$

where J_{ion} is RC ion flux intensity, n_H is neutral H density, and σ_H is the hydrogen charge exchange cross section. To obtain the global ion distribution requires deconvolution of J_{ion} from this line integral, which can be accomplished by mathematical inversion or forward modeling (Brandt et al., 2001a; Brandt, Ohtani, et al., 2002; Perez et al., 2001, 2004). TWINS stereo imaging obtains multiple LOS through the same ENA source distribution, providing a better constrained deconvolution of the high-altitude, trapped ring current (section 2.1).

Unlike the optically thin RCE region, ENAs emerging from below 800 km altitude are particles that have undergone many charge exchange and stripping interactions with the much denser neutral oxygen (O) exosphere. These ENAs make up the so-called LAE, given by the more general equation

$$J_{\text{LAE}} = \sigma_O \int_{\text{LOS}} n_O \, J_{\text{ion}} \, \exp[-\tau] dS, \qquad (2)$$

in which $\tau \equiv \sigma_S \int_0^S n_O \, dS$ is the ENA optical depth, n_O is neutral O density, σ_O is the oxygen charge exchange cross section, and σ_S is the stripping cross section (for conversion of ENAs to ions). This equation was used by Bazell et al. (2010) to develop the thick-target approximation (TTA), a mathematical treatment of ion-neutral interactions in the optically thick region that permits the extraction of ion data from LAEs in ENA images (section 2.2).

1.2.2. Lyman-α Imaging Technique

Figure 2d illustrates the TWINS Lyman-α imaging technique. Each imager consists of two 4° × 4° sensors, oriented 40° away from the actuator rotation axis (i.e., approximately the Earth nadir line). The actuator motion sweeps out an annular cone covering 4° × 360°. Multiple measurements of Lyman-α geocoronal glow from different vantage points along the TWINS orbit are collected and are used to create a parameterized empirical model of the neutral H density (Bailey & Gruntman, 2011; Nass et al., 2006; Zoennchen et al., 2010, 2011).

1.3. Open Questions Prior to TWINS

The IMAGE mission demonstrated that obtaining macroscale ion distributions—on time scales of minutes to hours—is essential to confirm hypotheses, make discoveries, and refine models (Brandt, Ohtani, et al., 2002; Burch, 2003; Burch et al., 2001; Fok et al., 2003). In situ data could only provide a statistical picture of this macroscale structure (Denton et al., 2005; Garcia & Spjeldvik, 1985; Lui et al., 1987, 1990). At the start of the TWINS geospace imaging mission, open questions about the ring current remained in many topic areas.

1. *What is the global distribution of trapped RC ions?* Before TWINS, monoscopic ENA imaging had yielded ion deconvolutions with more limited dimensionality and structure. ENA-derived ion flux distributions contained very little mesoscale or fine-scale structure (e.g., Brandt, Ohtani, et al., 2002; Brandt, DeMajistre, et al., 2002), even though in situ data had revealed significant local structure (e.g., Kistler et al., 1989). Global ion PADs were obtained in a few cases, but were usually assumed to be isotropic (Brandt et al., 2002; Lui et al., 2005; Perez et al., 2001). The zero-order knowledge of global ions (flux, PADs) obtained from IMAGE needed development. Single-spacecraft imaging from an elliptical polar orbit also made continuous observations (from storm commencement to recovery) difficult or impossible.

2. *What are the global, dynamical, energy-dependent linkages between trapped and precipitating ions?* This question involves trying to understand when, where, and why ion precipitation occurs. The first ENA images by the International Sun-Earth Explorer 1 and Polar contained both low- and high-altitude signals, but at extremely low spatial resolution (Roelof, 1987; Roelof et al., 1985; Henderson et al., 1997). Astrid microsatellite observations of low-energy (≤10 keV) LAEs were used to infer the high-altitude trapped ion distribution (Brandt et al., 2001a, 2001b), but RCE measurements were not available to constrain or validate the ion estimates. IMAGE provided the first high spatial resolution images containing both LAEs and RCEs. However, owing in part to the difficulty of interpreting the optically thick region, LAEs were rarely considered in analysis of IMAGE data (Pollock et al., 2009). Thus, prior to the development of TTA analysis (equation (2) LAEs were an underutilized resource for studying the connections between the ring current and ionosphere.

3. *How does global ion temperature vary in space and time versus storm phase, storm type, and solar cycle?* Analysis of local data has revealed important trends in plasma sheet ion temperature, such as higher temperature near dusk than dawn, colder temperatures during northward IMF, and increased temperature during fast earthward flows (Birn et al., 1997; Borovsky et al., 1997; Terasawa et al., 1997; Thomsen et al., 2003; Wang et al., 2006; Zhang et al., 2005). While these measurements are essential to understand local heating, they do not easily reveal how regional heating and cooling depend on solar wind driving conditions, storm phase, storm type, and solar cycle.

4. *How does global ion composition evolve during storms?* In situ ion composition data had shown that O^+ can dominate the phase space density and energy density of the ring current, especially during the main phase of large storms (Daglis et al., 1993, 1999; Hamilton et al., 1988; Kistler et al., 1989). However, these local measurements could not determine the timing or conditions of O^+ global injection and loss. The IMAGE mission obtained the first composition-separated ENA images, in the 52–180 keV range, which showed that these higher-energy O^+ ions are injected on substorm time scales (Mitchell et al., 2003). Still unknown were

the dynamics of O^+ below 50 keV and the systematic dependence of ring current O^+ ions (at all energies) on storm strength and storm phase.

5. *What is the global distribution of the extended neutral H exosphere?* Monte Carlo simulations had predicted that the neutral H exosphere should exhibit significant asymmetries in latitude and local time, and a solar-driven time dependence (Hodges, 1994). Spatial asymmetries and time dependence were indeed observed during the strong SC 23 solar maximum, by the LAD on board the IMAGE spacecraft (Østgaard et al., 2003). Despite these results, many ENA inversions of the IMAGE era assumed a spherically symmetric and time-static exosphere (Rairden et al., 1986), underestimating the neutral H density especially on the nightside. This error can lead to artificially high ion fluxes in inversion results such as those reported by Vallat et al. (2004). Moreover, an updated exosphere model was necessary for the TWINS era, because the solar maximum model of Østgaard et al. (2003) was not valid for the much weaker solar activity that prevailed after 2008.

2. Scientific Results From 2013 to 2017

Since commencing routine ENA and Lyman-α imaging in 2008, TWINS has monitored the last part of the deep minimum of solar cycle (SC) 23, and the moderate maximum of SC 24, observing geospace conditions ranging from extremely quiet to major storms such as the 2015 St. Patrick's Day event. The first 5 years of TWINS observations (2008 to 2013) were reviewed by Goldstein and McComas (2013). This sequel review covers TWINS studies of the geospace response published during 2013 to 2017, with selected earlier results mentioned to provide context. The discussion is organized into seven major science topics in sections 2.1 through 2.7.

2.1. Global Distribution of Trapped RC Ions

TWINS uses a validated inversion method (section 1.2.1) to convert ENAs to global ion flux, pressure, and pitch angle distributions (Grimes et al., 2010; Perez et al., 2012). Taking advantage of either stereo imaging or continuous coverage available from two imagers, several investigations revealed new dependencies and global asymmetries of storm time PADs, and provided upper limits on lifetimes of ion anisotropy (Goldstein et al., 2012a; Grimes et al., 2013; Keesee, 2017; Perez et al., 2012).

Building on this previous work, Perez et al. (2015) demonstrated that stereo ENA imaging enables inversions that resolve multiple flux peaks in the ring current. Figure 4a shows 15 keV stereo ENA images from 1408 UT on 29 May 2010, shortly after the peak of a CME-driven storm. Figure 4b shows the inversion obtained from the stereo images at 1408 UT, which contains three distinct peaks. Simultaneous observation of multiple RC peaks requires imaging; this measurement simply cannot be made with any reasonable number of in situ spacecraft. Moreover, through comparison of side-by-side monoscopic and stereo inversions, Perez et al., 2015 showed that resolving all three peaks requires stereo imaging (both imagers). The additional information provided by two LOS per pixel enabled a better inversion in this study.

In Figure 4c is shown a quantitative comparison of TWINS inversions with simultaneous in situ data obtained by the three-spacecraft Time History of Events and Macroscale Interactions during Substorms (THEMIS) mission (Angelopoulos, 2008; Angelopoulos et al., 2008). The figure plots ion fluxes from THEMIS e (black curve), together with the ion fluxes from a sequence of four TWINS inversions (1338, 1353, 1408, 1423 UT, colored curves), sampled along the THEMIS e orbit. Though obviously the THEMIS data show more structure than TWINS (which intrinsically has lower spatial resolution), the overall trend is the same: after 1344 UT, flux increases with UT. From inspection of the sequence of inversions (cf. Perez et al., 2015), this flux increase was not a temporal change; rather, THEMIS e penetrated deeper into a quasi-static global RC peak. Comparison of TWINS imaging and THEMIS in situ data thus enabled separation of spatial and temporal effects.

Inversion-driven studies continue to advance our understanding of spatial, spectral, and pitch-angle (PA) structure of the ring current. Perez et al. (2016) applied their inversion analysis to the main phase of the large (−223 nT) geomagnetic storm that began on 17 March 2015. The derived ion flux distribution shows two premidnight peaks ("1" and "2" in Figure 5a). Whereas peak 1 (inside geosynchronous Earth orbit (GEO)) was quasi-static, the outer peak (2) fluctuated in time and eventually disappeared during storm recovery. As noted above, simultaneous observation of multiple RC peaks requires imaging.

Figure 5b shows another comparison of TWINS inversions with simultaneous in situ data, this time using flux measurements from the two-spacecraft Van Allen Probes mission, formerly known as Radiation Belt Storm Probes (RBSP) (Mauk et al., 2013). Hereinafter, we shall refer to the mission as Van Allen Probes,
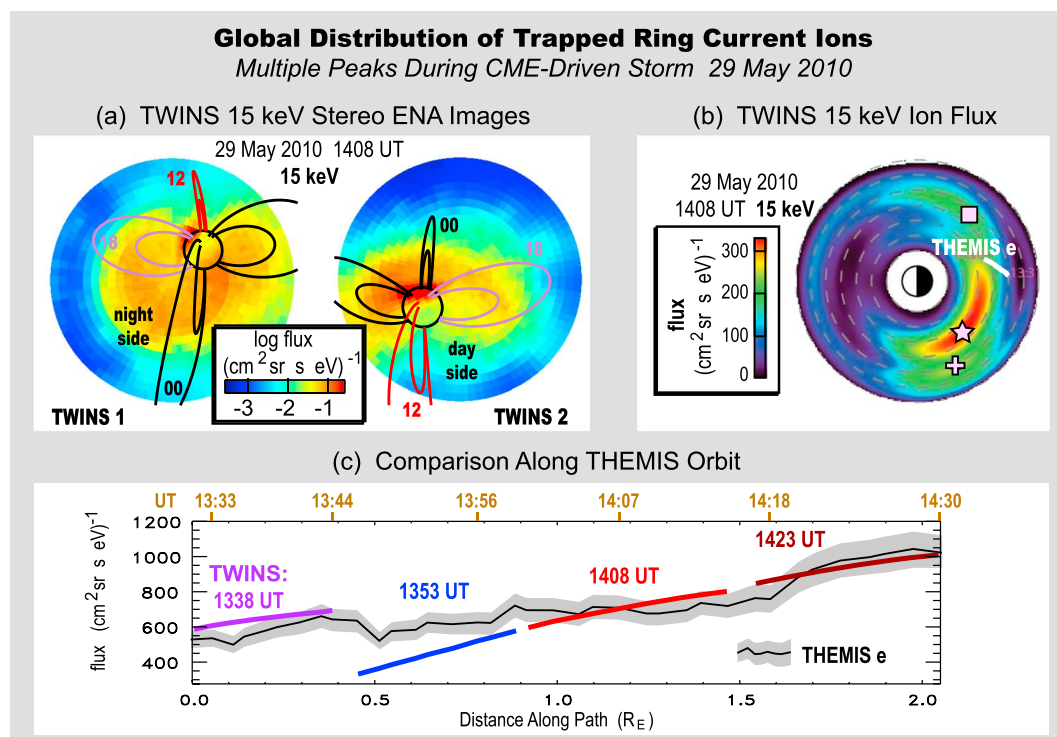
Figure 4. Two eyes are better than one. Stereo imaging reveals multiple ion peaks in the storm time ring current (Perez et al., 2015). (a) TWINS 15 keV stereo energetic neutral atom (ENA) images at 1408 UT on 29 May 2010. TWINS 1 and 2 viewed the ring current from the nightside and dayside, respectively. (b) Equatorial, 15 keV ion flux, obtained by mathematical inversion of stereo images from Figure 4a. Three peaks are identified (star, box, and plus symbols). Time History of Events and Macroscale Interactions during Substorms (THEMIS) e orbit during this time is shown. (c) Comparison of ion flux along THEMIS e orbit, from 1331 to 1430 UT on 29 May. Black curve: THEMIS flux. Color curves: TWINS ion flux for a sequence of four inversions (1338–1423 UT).

but the individual probes by their acronyms (RBSP A and RBSP B). Figure 5b plots RBSP A ion flux and PA anisotropy (black curves), with ion data from a sequence of TWINS inversions (red curves) sampled along the RBSP A orbit. As with the THEMIS comparison above, the RBSP A data show more structure than TWINS, but the global two-peak structure is evident in both measurements. Note that the RBSP A orbit does not traverse the exact location of each global peak in the inversion. For example, peak 1 occurs about 2 h east of dusk MLT, but RBSP A crosses the L shells of the partial RC closer to midnight MLT. Given the peak 2 temporal fluctuations observed by TWINS, some of the peak 2 variability measured by RBSP A is temporal.

TWINS ion inversions are helping to understanding the pitch angle distributions of the storm time RC. The global PA anisotropy (Figure 5b) was perpendicular (as expected) inside GEO, but more field aligned at large radial distances. Using global modeling, this regional spatial structure was explained as evidence of ion drift in a region of highly nondipolar field (section 2.6). Interpretation of global PADs thus reveals important details about regional ion transport. Regarding the global-local agreement in Figure 5b, Perez et al. (2015) had demonstrated that stereo imaging more accurately resolves flux peaks. The newer result by Perez et al. (2016), using only TWINS 1, shows how single-point inversions can still achieve reasonable agreement — in both flux and PAD — with in situ data.

Consistent with the analysis cited above, the cross-scale ion energetics also suggest that RC injection is a bursty, structured process. Goldstein et al. (2017) used inversions from this same 17 March 2015 storm to investigate the global structure of ion spectra. Their cross-scale analysis was performed using three missions together: TWINS, Van Allen Probes, and THEMIS (section 2.7). They found multiple spectral peaks in both the ENA inversions and the in situ data. Structured ion spectra have been previously interpreted as resulting from multiple-substorm dipolarizations and other solar wind-driven changes in the convection field (Ebihara et al., 2004; Li et al., 2000).
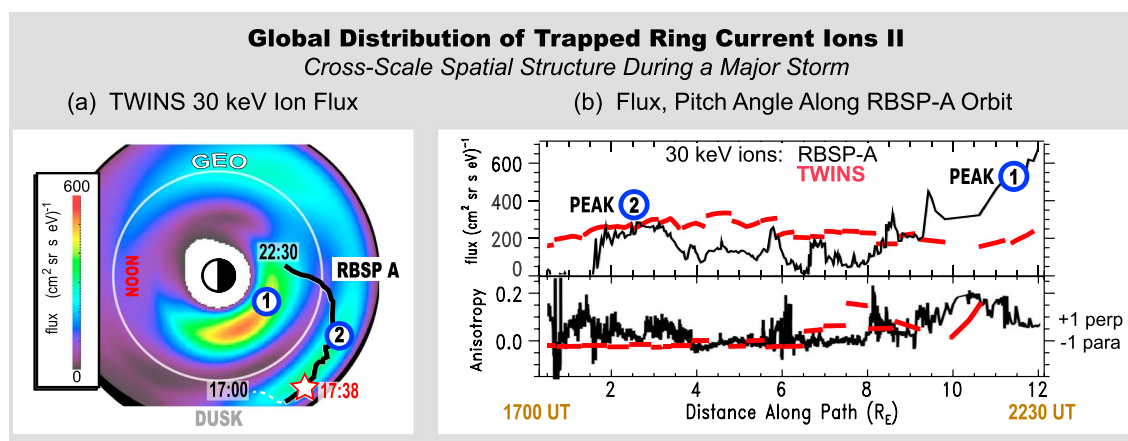
Figure 5. Cross-scale flux and pitch angle structure. TWINS and Van Allen Probes (RBSP) data reveal the complexity of ring current structure (Perez et al., 2016). (a) Equatorial, 30 keV ion flux at 1738 UT on 17 March 2015, obtained by mathematical inversion of TWINS 1 data. Two peaks are found ("1" and "2"). RBSP A orbit (black line) and its 1738 UT location (star) shown. (b) Ion flux and pitch angle anisotropy along RBSP A orbit, from 1700 to 2230 UT on 17 March. Comparison of RBSP (black) and TWINS (red) data confirms two global peaks ("1" and "2") and that each large-scale peak comprises smaller-scale structures.

Ion inversion methods have been continually reexamined and/or improved as the TWINS mission has matured. Ma et al. (2015) developed an alternate, tomographic inversion method that agrees (both absolute flux and spectral shape) with simultaneous THEMIS data. Other TWINS studies have applied simplified inversion techniques to extract ion flux information with less computational expense and complexity (Goldstein et al., 2012b; Goldstein et al., 2012a; Valek et al., 2015).

These results advance our knowledge of the global RC ion distribution. Macroscale RC injections are made up of a collection of bursty, spatially structured regions of intensified flux. Each global peak in the RC comprises a great deal of finer-scale spatial structure. Multiple ion peaks and regions can have distinctly different time-dependent spectra from each other and different PADs. The inclusion of models (Goldstein et al., 2017; Perez et al., 2016) can reveal the action of physical mechanisms such as regional variations in the geomagnetic field that affect pitch-angle-dependent transport and convection onset (section 2.6). Stereo imaging reveals more spatial structure than monoscopic imaging, but still less than local measurements.

2.2. Low-Altitude Ion Precipitation

Made possible by the TTA method (Bazell et al., 2010), ion flux information from the LAE signal has proven to be a valuable means of revealing the global spatial/temporal dependence and energetics of ion precipitation (Buzulukova et al., 2013; Goldstein et al., 2013; LLera et al., 2012; McComas et al., 2012; Valek et al., 2010, 2013). Several recent TWINS studies have continued this progress.

Earlier results had verified that LAEs are highly directional and sharply peaked versus MLT along the limb (Bazell et al., 2010; Goldstein et al., 2013; Pollock et al., 2009). For example, Figure 6a shows a close-up of an LAE from 1131–1145 UT on 6 April 2010; the flux is concentrated at the opposite Earth limb from TWINS, in this case centered at 2235 MLT (labeled "LAE peak"). This directionality comes about because ions mirroring at low altitudes have sharply peaked PADs, and so do their ENAs. The intensity of the LAE depends strongly on the pitch angle (α) sampled by the LOS (Figure 6b). Goldstein et al. (2016) estimated the peaked ENA PADs using a Monte Carlo simulation of the proton aurora (Figure 6c). As energy increases, the PAD becomes broader (less anisotropic) and shifts toward more upwardly directed ENAs. If the LOS (yellow vertical bar) does not sample the peak of the PAD, the observed intensity is artificially dimmed. The analytical correction for this viewing geometry effect consists of dividing by the normalized PAD for the LOS. The correction yields much improved agreement with simultaneous National Oceanic and Atmospheric Administration (NOAA) 17 satellite ion fluxes (Figure 6d), a factor of 7 better than the uncorrected fluxes. Even with this improvement the agreement is still imperfect, as indicated by the color mismatch between the NOAA and TWINS points for peaks A and B in the figure. Fluxes derived from imaging pixels are generally expected to be artificially low because subpixel structure is averaged or smoothed out. Goldstein et al. (2016) found that fluxes obtained from 1° pixels can be twice as high as those from larger 4° pixels.
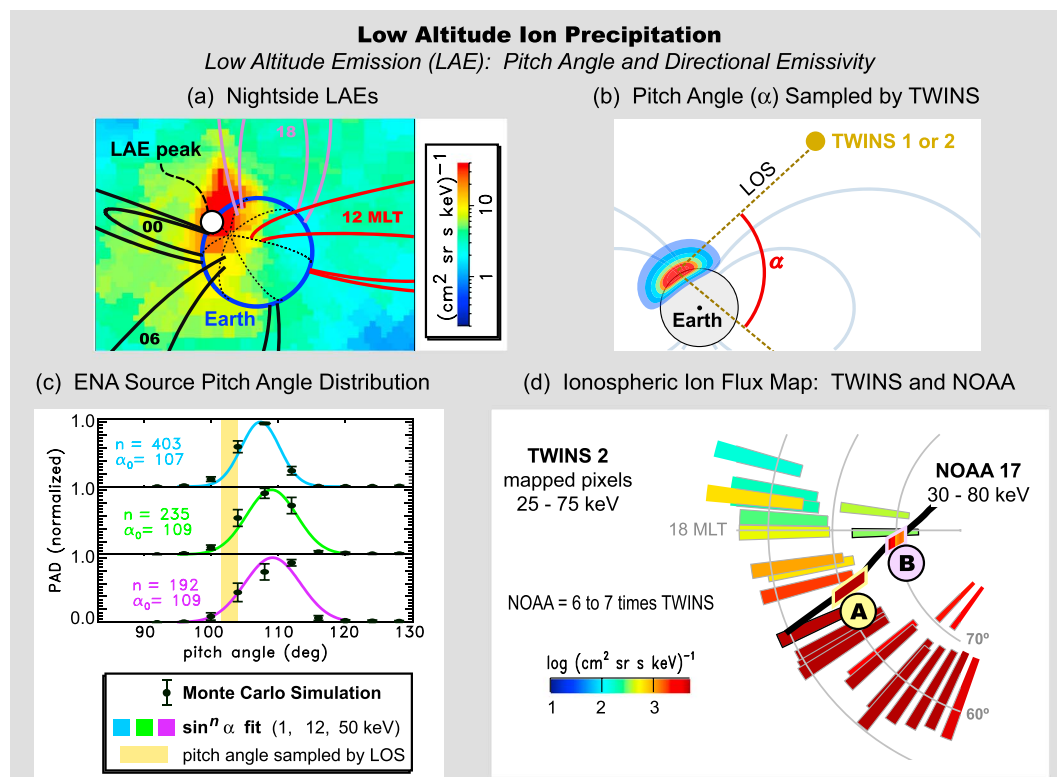
Figure 6. Quantifying global ion precipitation. Low-altitude emission (LAE) viewing geometry correction, developed and validated (Goldstein et al., 2016). (a) TWINS 2 energetic neutral atom (ENA) image (50 keV) containing an LAE with peak at 2235 MLT. (b) Viewing geometry for LAEs. The intensity of the LAE depends strongly on the pitch angle (α) sampled by the line of sight (LOS), because ENA pitch angle distributions (PADs) are sharply peaked. (c) Normalized ENA pitch angle distributions at (1, 12, and 50) keV, from a Monte Carlo simulation (black dots) and fitted to a $\sin^n \alpha$ function (color curves). Viewing geometry correction consists of dividing by normalized PAD. (d) Comparison of corrected ion flux from TWINS (mapped pixels) and NOAA (along trajectory), plotted using same color bar. Regions A and B are broad proton peaks observed by NOAA.

Valek et al. (2014, 2018) examined the time development of both LAEs and MLT-dependent ring current enhancements, for several large (Dst < -100 nT) storms and studied causal connections between trapped and precipitating ions. For example, in the double-dip 17 March 2013 storm, they found that although LAEs track the trapped distribution in time, the relative LAE flux intensity increased by an order of magnitude between storm commencement and the first storm peak. For the second storm peak, the relative LAE intensity decreased. These observations indicate a full loss cone during the first peak but not the second. Observations from the main phases of the selected storms also exhibit an energy dispersion in both the precipitating and trapped populations.

LAEs are useful to understand dynamic linkages among different magnetospheric regions. Using multimission data side by side with models, Buzulukova et al. (2018) correlated in situ ion flux dropouts observed by RBSP A with simultaneous dimming of global LAE intensity, meaning that the local dropouts reflect macroscale changes in RC flux (cf. section 2.6). Goldstein et al. (2017) used TWINS LAEs to determine the MLT and energy dependence of precipitating ion flux during the major 17 March 2015 storm (cf. section 2.7). They found that an isolated injection triggered a subsequent cooling of the LAE-derived ion spectra. The implication is that substorms can play an important role in storm recovery by injecting cooler ions into a preexisting hot RC.

Analysis of LAEs has also advanced understanding of low-altitude ion-neutral interactions. LLera et al. (2017) used a novel analytical approximation to a full transport code to study the energy loss experienced by particles in the thick-target region where LAEs are generated. Precipitating ions undergo multiple charge-exchanging interactions, and each such interaction incurs an energy penalty of ∼36 eV (Dalgarno, 1962; Dalgarno & Griffing, 1958). For few keV LAEs the cumulative loss can be a significant fraction of the energy of the initial precipitating ion. LLera (2017) applied this energy correction to a low-altitude precipitation event previously

studied by Bazell et al. (2010) and found good agreement with the in situ spectrum. These two studies concluded that multiple charge-exchanging interactions strongly couple the ions and ENAs together, so that precipitation can be viewed as a joint ion-neutral process.

Ion precipitation is an essential component of system-level RC dynamics, so inversion algorithms must incorporate LAEs into their framework (Perez et al., 2012; Ma et al., 2015). As noted earlier (section 2.1 and Figure 5a), during the 17 March 2015 storm TWINS measured a two-peak structure in the trapped RC. Goldstein et al. (2017) linked the second RC peak, outside geosynchronous orbit, to the LAEs at that time. This second peak is also evident in the RBSP A data (Figure 5b). Thus, more accurate ion distributions (that agree with in situ data) require inclusion of LAEs into the inversion results.

2.3. Global Ion Temperature

A dynamic system-level picture of magnetotail temperature is needed to understand heating and cooling during the ring current injection process. To meet this need, global temperature maps were developed for TWINS by Keesee et al. (2011, 2012), based on earlier work by Scime et al. (2002).

Elfritz et al. (2014) and Keesee, Chen, et al. (2014) validated the technique by showing agreement with simultaneous THEMIS data. In Figure 7a, TWINS energy flux (versus energy) is in excellent agreement with corresponding data from THEMIS a. Figure 7b compares TWINS-derived temperatures with those of THEMIS a. The TWINS-derived temperatures are closer to those of THEMIS than the commonly used TM model (Tsyganenko & Mukai, 2003), which has implications for global modeling (cf. section 2.6). The good agreement not only validates TWINS temperature analysis, but it also shows the global-to-local relationship. As mentioned in section 2.1, global features (like peaks in the measured quantity) seem to comprise a great deal of finer-scale structure.

TWINS ion temperature maps during the transition from SC 23 (solar minimum) to SC 24 (rising phase) have revealed a dramatic difference between geomagnetic storms driven by CMEs versus those driven by CIRs. Keesee, Elfritz, et al. (2014) performed the first superposed epoch analysis of global ion temperature, for an ensemble of CIR and CME storms. They analyzed 48 storms between June 2008 and April 2012, and found that each type of storm driver yields different dynamics (Figure 7c). To complement this analysis and aid interpretation, the Comprehensive Ring Current Model (CRCM) of Fok et al. (2001) was run for a subset of storms. (CRCM is described more fully in section 2.6.) Stronger convection during CME storms transports higher-energy ions closer to Earth, producing higher temperatures than for CIR storms. During intense CME storms, magnetopause compression causes the highest temperatures at storm onset, followed by a main phase decrease. Moderate CME storms have relatively steady temperatures from start to finish. As shown in Figure 7c, temperatures during the early main phase of moderate CME-driven storms are up to 80% higher than for CIR storms. Updated analysis by Keesee et al. (2017) confirmed dramatically varying temperature dynamics for different storm types.

Katus et al. (2017) used superposed epoch analysis on a different ensemble of 48 storms spanning July 2009 to December 2015 (Figure 8a). The resulting temperature maps (e.g., Figure 8b) highlight dramatic system-level changes—regional heating and cooling—during storms. Between 14 h and 17 h the entire nightside experiences heating: average global temperatures rise from ~5.5 keV to ~7.5 keV. A few hours later (20 h) the duskside plasma sheet remains hot while the dawnside cools to <6 keV, most likely caused by energy-dependent westward ion drift. In Figure 8c Geotail-derived average temperatures are compared with those from TWINS (sampled along Geotail orbits); the root-mean-square error is <3 keV, and the 6 h averaged trends are very similar. Katus et al. (2017) also reported favorable comparisons of TWINS-derived temperatures with Los Alamos National Laboratory (LANL) geosynchronous data (McComas et al., 1993); near the peak of the storm, both local and global measurements indicate a ~3 keV minimum temperature near dawn.

TWINS temperature maps have consistently contained global plasma sheet gradients (Keesee, 2017). These macroscale temperature gradients are proving to be valuable for constraining and validating global models. Quiet-time temperature maps by Keesee et al. (2011) confirmed the presence of a quiescent dawn-dusk asymmetry, predicted by Spence and Kivelson (1993). Keesee and Scime (2015) published on CDAWeb (i.e., Coordinated Data Analysis Web; Candey et al., 2012, http://cdaweb.gsfc.nasa.gov) a database of TWINS temperature maps for 76 geomagnetic storms between 2008 and 2013, to provide system-level context for in situ measurements and furnish time-dependent boundary conditions for global models, e.g., as done by Elfritz et al. (2014).
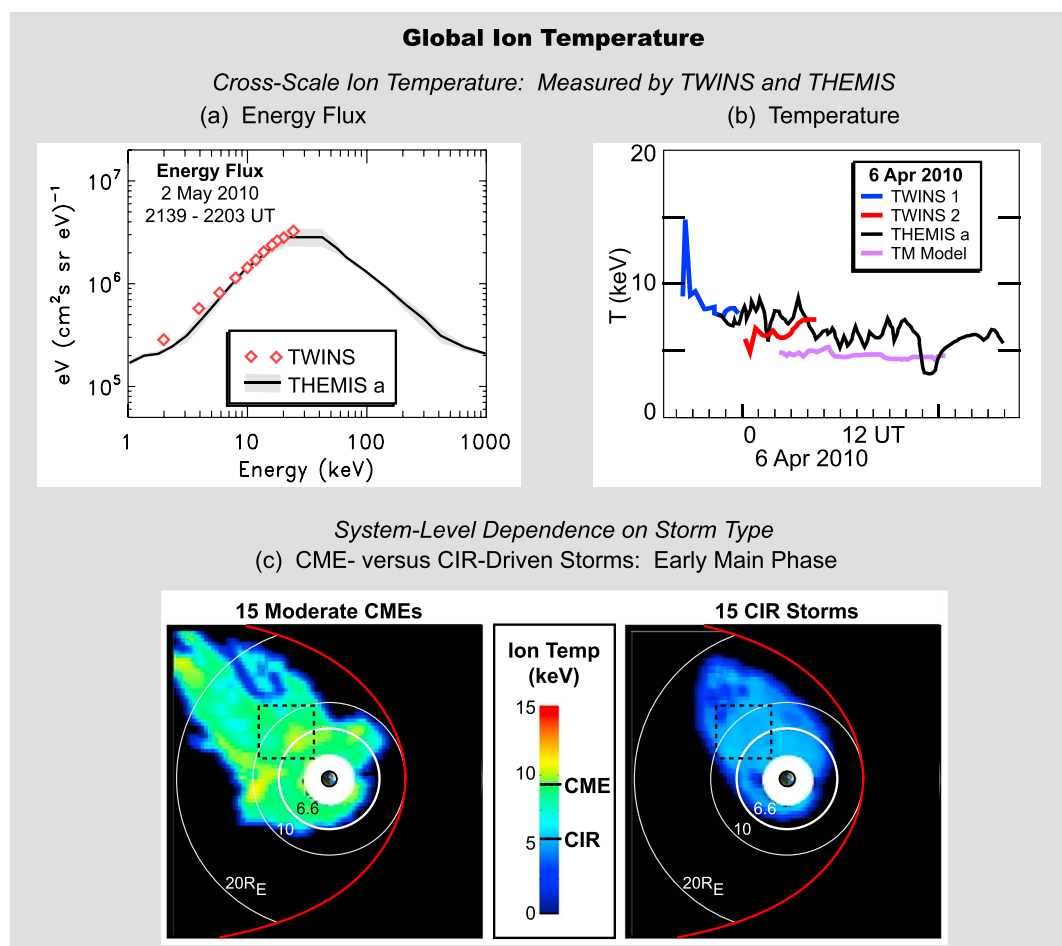
Figure 7. Global magnetospheric ion temperature. TWINS ion temperature maps reveal system-level magnetospheric heating and energization (Keesee, Chen, et al., 2014; Keesee, Elfritz, et al., 2014). (a, b) Comparison of TWINS-derived energy flux and temperature with those of Time History of Events and Macroscale Interactions during Substorms (THEMIS) a. TWINS temperatures are in closer agreement than the Tsyganenko and Mukai (2003) model. (c) Superposed epoch analysis of coronal mass ejection (CME)- versus corotating interaction region (CIR)-driven storms, showing significantly higher temperatures for CMEs. The average temperatures inside the dashed boxes are indicated in the color bar: 5–6 keV (CIR), 8–9 keV (CME). The red curve in each plot is a reference magnetopause given by the model of Shue et al. (1997), with $r_0 = 10\ R_E$ and $\alpha = 0.65$.

These results represent an important step forward in understanding the dynamics of global ion heating throughout a storm, for different storm types and different parts of the solar cycle. The TWINS-CRCM comparisons establish links between particle transport and temperature and between plasma sheet and ring current dynamics. The system-level perspective is important to understand causal relationships and help improve models.

2.4. Ion Composition

Oxygen and hydrogen species-separated images (e.g., Figure 9a) permit the study of global ion composition in the ring current. The High-Energy Neutral Atom camera on board IMAGE used detector pulse height analysis to obtain the first oxygen ENA images in the high-energy range, above 50 keV. (Mitchell et al., 2003). TWINS extended that capability down to medium energies, i.e., 16 to 50 keV (Valek et al., 2013). Recently, experimental data using the TWINS engineering model (EM) was used to extend the pulse height analysis from its former upper limit of 50 keV, to include the TWINS instrument's full range of 1–100 keV for H ENAs, and 16–256 keV for O ENAs (Delmonico, 2015). This expanded capability was first applied to the major storm of 17 March 2015 (peak Dst −223 nT). Figure 9a shows examples of the resulting composition images from 1744 UT (i.e., storm main phase), at three energies: 16, 64, and 128 keV. The flux color scale is the same for all six images. As expected for a large storm, TWINS measured significant oxygen flux across the nightside, especially near midnight.
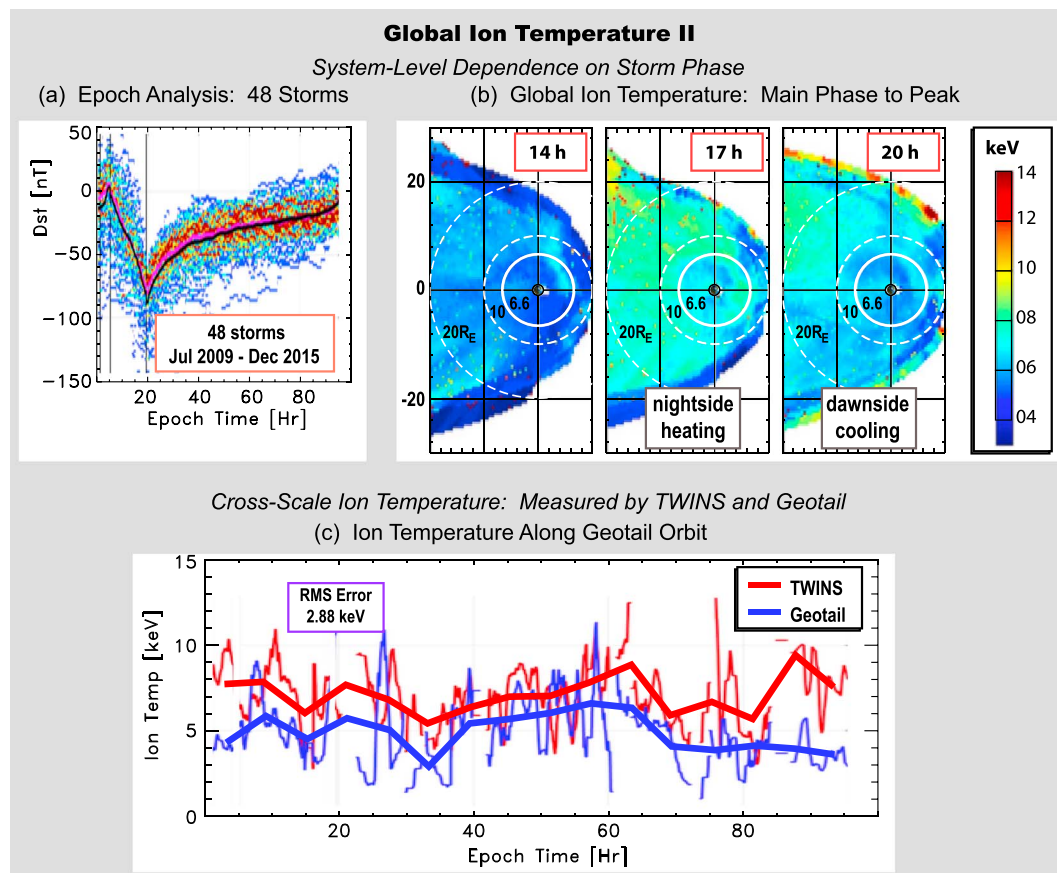
Figure 8. Dependence on storm phase. Statistical view of TWINS ion temperatures (Katus et al., 2017). (a) Superposed epoch analysis of Dst for 48 storms (July 2009 to December 2015). Storm commencement is defined as 0 h epoch time. (b) Forty-eight storm average temperature maps (in geocentric solar magnetospheric coordinates) at three epoch times during the main phase. Global temperature increases across nightside, then migrates duskward. (c) Comparison with Geotail data; thick lines are 6 h smoothed averages of the thin lines.

Recent work using such images has addressed key aspects of the magnetospheric ion composition question. Valek et al. (2014) performed a statistical, superposed epoch study of how H versus O composition evolved during nine large (Dst < -100 nT) storms of SC 24. Their method used H and O ENAs as proxies for the corresponding ion concentrations. Figure 9b shows global composition versus storm phase. Compared to high-energy (above 50 keV) oxygen (Mitchell et al., 2003), which exhibits global changes on substorm (minutes) time scales, medium-energy O evolves on storm (hours to days) time scales. The pathway for ionospheric O^+ to enter or leave the ring current is thus slower for medium energies (16–50 keV). Valek et al. (2014) also looked at the storm phase dependence of energy spectra for both H and O, and found a species dispersion: 32 keV H ENAs increased in flux before the arrival of 32 keV O ENAs, and the O ENAs took longer to reduce to prestorm levels during the storm recovery phase. Keesee (2017) and Valek et al. (2014) also noted a dawn-dusk asymmetry favoring higher O^+/H^+ near dawn, caused by a reduction in H^+ there.

This statistical result was extended by Valek et al. (2018) to include the major 17 March 2015 storm (Figure 9c), and apply the recently increased energy range (Delmonico, 2015). Their method includes obtaining ion concentrations via a simplified deconvolution (section 2.1), which takes advantage of the common LOS shared by each pixel of an H or O ENA image. Figure 9d plots oxygen ion concentration O^+/H^+, at 16, 64, and 128 keV, plotted versus geomagnetic activity as represented by the SymH index. Data are separated into prepeak (blue) and postpeak (red) bins. These three plots show several remarkable trends. First, the O^+/H^+ ratio at the strongest SymH values (i.e., at the peak of the strongest storm, the 17 March event) decreases by nearly 2 orders of magnitude (from ~1 to ~0.05) between 16 keV and 128 keV. Second, for weaker values of SymH (either early main phase or recovery) the highest-energy O^+/H^+ increases above ~0.5. Thus, the most
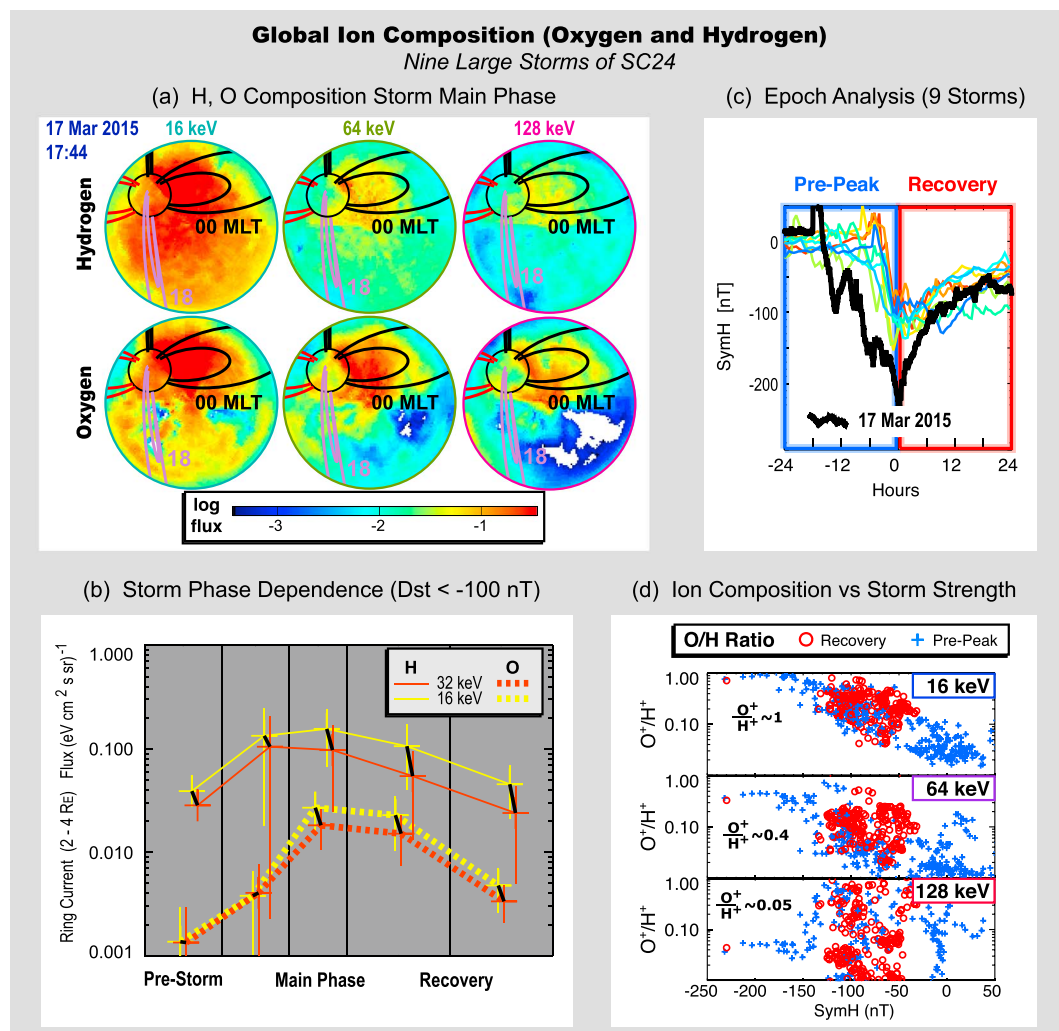
Figure 9. System-level ion composition. TWINS species-separated images reveal how O^+/H^+ depends on storm phase and strength (Delmonico, 2015; Valek et al., 2014, 2018). (a) H and O energetic neutral atom (ENA) images at three energies during late main phase (1744 UT) of the major storm on 17 March 2015. (b) The storm phase (epoch) dependence of composition (using H and O ENAs as proxies for H^+ and O^+) for two energies. (c) Epoch analysis of nine large (Dst ≤ -100 nT) storms from solar cycle (SC) 24; the black trace is 17 March 2015. (d) For the nine large storms, the O^+/H^+ ratio versus SymH, for three energies, separated into before (blue) and after (red) the peak per storm SymH.

energetic O^+ ions in the ring current occur not at the peak of the storm, but rather either before or after the peak. Goldstein et al. (2017, cf. section 2.7) observed similar storm time energetics in their joint THEMIS-Van Allen Probes-TWINS study of the 17 March storm: the most energetic ions were observed early in the main phase rather than at the storm's peak. It is noteworthy that at the lowest medium-energy bin (16 keV) the O^+/H^+ ratio for large SymH is nearly 1, indicating major mass loading of the ring current. Valek et al. (2018) also examined the relative timing of trapped (RCE) and precipitating (LAE) oxygen and hydrogen (cf. section 2.2). They found that LAEs have a large increase in the O^+/H^+ ratio from prestorm levels, systematically for the large events analyzed and distinct from earlier results for smaller, CIR-driven storms (e.g., Valek et al., 2010).

TWINS composition-separated ENA images have been used with both in situ data and models to improve understanding. Valek et al. (2015) performed the first joint mission study between TWINS and the Van Allen Probes (cf. section 2.7). In addition to being the first global-to-local comparison of inner magnetospheric, medium energy ion composition, this study found a notable MLT and storm phase dependence to H^+ and O^+. Oxygen concentration was observed (in both images and in situ data) to increase near midnight during the main phase. Closer to the peak of the storm the oxygen concentration increase widened to encompass the entire nightside. Global regions of O^+ were found to comprise islands of smaller structure.

Ilie, Skoug, Valek, et al. (2013) compared TWINS oxygen images with a global model and found that plasmoids may be a major mechanism for O^+ transport and loss.

These recent TWINS composition results provide an expanded, systematic determination of the storm phase and geomagnetic activity dependence of global magnetospheric ion species. The relative timing of composition-separated LAEs versus RCEs provides insight into the energy-dependent time scales and pathways for global O^+ transport.

2.5. Neutral Exospheric Hydrogen

The TWINS LADs measure the geocoronal glow from neutral exospheric hydrogen atoms. This measurement complements TWINS ring current science in two obvious areas. First, knowledge of neutral H density is needed for quantification of charge exchange, which is a major loss term for the ring current. Second, accurate neutral H density distributions are essential for interpretation or inversion of ENA images (cf. section 2.1 and Ilie, Skoug, Funsten, et al., 2013). Recent Lyman-α imaging results also have revealed some surprising structure and dynamics of the neutral H exosphere.

TWINS LAD analysis constitutes formulating parameterized empirical models of neutral H density, based on the Lyman-α measurements (Nass et al., 2006; Zoennchen et al., 2010). Various LAD-based density distributions have characterized different aspects of the global H dynamics, including a solar minimum model (Zoennchen et al., 2011), a single-day model (Bailey & Gruntman, 2011), and a seasonally dependent model (Zoennchen et al., 2013).

Zoennchen et al. (2015) produced an empirical model characterizing how the neutral H exosphere changes over the solar cycle. They used LAD data from summer solstice 2008 and 2010 to obtain the solar minimum model shown in Figure 10a, valid between 3 and 8 R_E. Compared to their previous solar minimum model (Zoennchen et al., 2011), the updated model reveals new north-south, day-night, and dawn-dusk asymmetries. A solar maximum model (Figure 10b), based on LAD data spanning October–December 2012, extends farther into geospace than during solar minimum, because higher temperatures cause thermal expansion of the exosphere. This result was the first 3-D global, observation-based model of the solar-cycle-driven thermal expansion and contraction of the neutral H exosphere. A review by Keesee (2017) also noted a dawn-dusk asymmetry favoring higher-H density near dawn, at both solar minimum and maximum. To produce their solar-cycle model, a Monte-Carlo simulation was developed to treat multiple scattering effects, but which may also be used to help understand the relative contributions of ballistic, orbiting, and escaping atoms to the exospheric distribution.

A study by Bailey and Gruntman (2013) found H density increases of 5–15% on several-hour time scales (correlated with Dst) during geomagnetic storms. Zoennchen et al. (2017) also examined the effect of solar wind on the neutral H exosphere. As an index of the dynamics of neutral H, they used changes in Lyman-α (proportional to the LOS-integrated density). Careful subtraction of two background sources was performed. The first source is interplanetary ultraviolet light measured by the Solar and Heliospheric Observatory. The second source is solar irradiance variations measured by Thermosphere, Ionosphere, Mesosphere Energetics and Dynamics, Solar Dynamics Observatory, and Upper Atmosphere Research Satellite and compiled by the Laboratory for Atmospheric and Space Physics. For eight storms initiated by significant solar wind pressure increases ($P_{SW} > 7$ nPa, as given by the arrows in Figure 11), the exospheric density was found to increase by 9% to 23%. The exosphere responds on two time scales. First, there is an immediate rise in Lyman-α as soon as P_{SW} starts to increase. Second, several hours later the Lyman-α intensity reaches its peak. This time delay was found to be 11 h on average. Multiple P_{SW} peaks also produce multiple peaks in Lyman-α. This strong P_{SW} correlation is consistent with the earlier Dst correlation of Bailey and Gruntman (2013), but the newer result establishes a stronger link to a specific physical mechanism. Zoennchen et al. (2015) hypothesized that a rapid rise in P_{SW} compresses the magnetosphere and deposits energy into the lower exosphere, which triggers upward transport and thus increases the H density at high altitudes. It was also observed that the geocoronal tail above 8 R_E is better aligned with the solar wind than with the Sun direction, indicating particle contributions from outside the magnetosphere. The TWINS Lyman-α results represent a growing body of evidence that the solar wind can be a major driver of neutral exospheric density.

TWINS Lyman-α imaging captures very important global exospheric dynamics affected by Sun, solar wind, and geomagnetic activity. The solar cycle (SC)-dependent model is a significant advance from previous models. Knowledge of SC-dependent global asymmetries impacts ring current and ENA imaging science. Neutral H
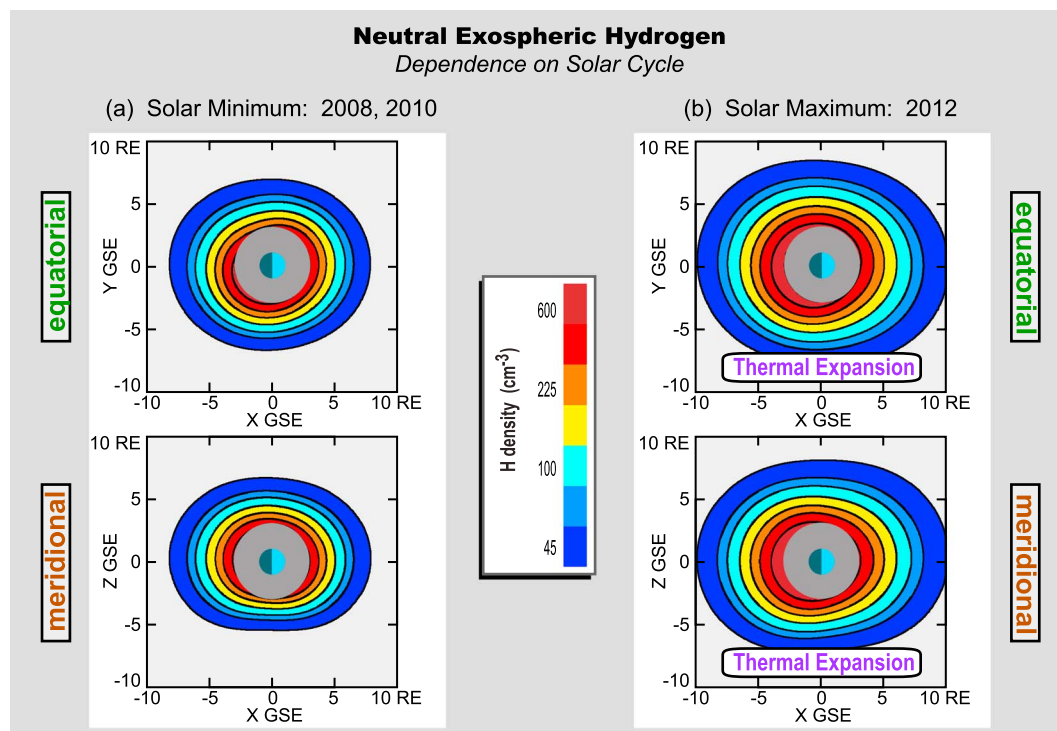
Figure 10. Neutral exospheric hydrogen versus solar cycle. TWINS Lyman-α imaging has characterized the solar cycle dependence of the neutral H exosphere (Zoennchen et al., 2015). (a) Solar minimum: TWINS Lyman-α detector data from solstice 2008 and 2010. Contours of neutral H density are shown in the GSE equatorial and meridional planes. (b) Solar maximum (October–December 2012): the exosphere is expanded by higher temperature.

density enhancement (either in the form of subglobal structure or global thermal expansion) can raise the charge exchange loss rate and produce more ENAs for imaging.

2.6. Global Modeling

An effective way to study the global geospace response is side-by-side interpretation of images and models. The global constraints provided by images can help models produce more realistic results. Physics-based models offer a means of interpreting the images to discover which mechanisms are controlling the dynamics. Numerous TWINS-based studies have included global models in this way (Buzulukova et al., 2010; Fok et al., 2010; Glocer et al., 2011; Ilie, Skoug, Valek, et al., 2013; McComas et al., 2012).

Fok et al. (2014) developed an augmented version of the well-known Comprehensive Ring Current Model (CRCM), called the Comprehensive Inner Magnetosphere-Ionosphere (CIMI) model, that now includes radiation belt physics. CIMI and CRCM compute phase space density (PSD) and flux distributions, field-aligned currents, convection potentials, and ionospheric precipitation; CIMI also calculates wave-particle interactions with radiation belt particles. Figure 12a compares simulated 2-D equatorial ion flux distributions for the 6 April 2010 CME-driven storm. Two CIMI simulation runs are shown, differing only by the convection electric (E) field used. One run uses the Weimer empirical E field (Weimer, 2001), and the other a self-consistent E field (SCE) that includes contributions from magnetosphere-ionosphere (M-I) coupling. A clear difference between these two runs is the MLT location of the RC peak. Using the Weimer empirical field produces a weak flux peak in the premidnight MLT sector, whereas the SCE puts a stronger peak in the postmidnight sector, closer to dawn. To judge which E field is more realistic, simulated ENA images (Figure 12b) were compared directly with TWINS data (Figure 12c). By inspection, using the SCE yields a simulated ENA image with its peak correctly located in the postmidnight MLT sector. This postmidnight skewing of the partial RC peak was first observed by IMAGE (Brandt, Ohtani, et al., 2002) and explained as resulting from distortion of the inner magnetospheric E field by M-I coupling (Fok et al., 2003). Only a SCE simulation can reproduce it. However, a later TWINS study by Buzulukova et al. (2010) noted that postmidnight enhancement of ENA flux could have additional contributions from MLT-dependent PADs or from the energy-dependent charge exchange cross section.
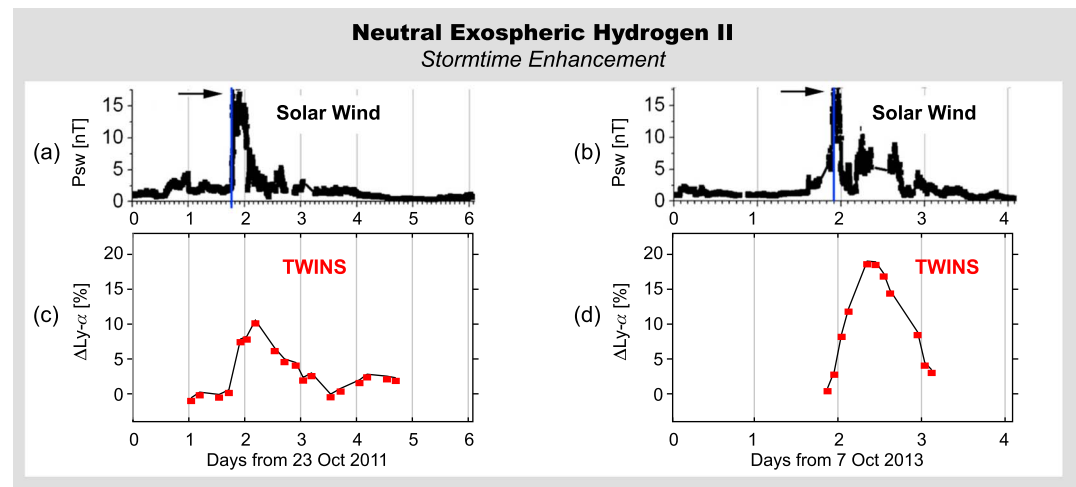
Figure 11. Solar wind influence on neutral exosphere. TWINS geocoronal imaging reveals correlation between solar wind pressure and the neutral H exospheric density (Zoennchen et al., 2017). (a, b) P_{SW}, solar wind pressure. (c, d) Change in Lyman-α brightness, proportional to change in line-of-sight-integrated density. Increased P_{SW} triggers exospheric density enhancements (up to 23%), with an average time delay of 11 h.

The model-data agreement shown in Figures 12b and 12c for the SCE increases confidence in CIMI's assessment of which physical mechanisms dominate the simulation. Figure 12d plots cumulative ΔE from ion drift (an energization term) and charge exchange or wave scattering (loss terms), which CIMI output indicates were the most important processes for this event. These results validate the importance of M-I coupling and self-consistent fields, and confirm that ion drift, charge exchange, and wave scattering are major influences on the RC . Fok et al. (2014) also compared CIMI output to Akebono energetic electron data to obtain some insight into how storms feed the radiation belts. They found that convection can increase relativistic electrons in the slot region, an unexpected result given that MeV electrons are dominated by magnetic drifts. They also confirmed the importance of very low frequency waves in energizing outer belt electrons.

TWINS ion temperature maps (section 2.3) can improve global geospace models by obtaining system-level data from the dynamic transition region outside geostationary orbit. Elfritz et al. (2014) used TWINS ion temperature data as a time-dependent boundary condition (BC) for the CRCM. They found that the spatial and spectral properties of the ring current are extremely sensitive to the choice of BCs. The left side of Figure 12e shows equatorial ion flux (at 12 keV) from the CRCM with temperature BCs specified two ways. The plot with the blue label shows the result of specifying BCs using the TM model (Tsyganenko & Mukai, 2003). The plot with the red label shows the result when BCs are specified using TWINS 2D temperature maps. When TWINS BCs are used, the flux is higher, and distributed over a wider range of MLT. The clear difference between these two flux distributions is resolved via comparison with THEMIS data. The right side of Figure 12e shows three energy flux spectra. The gray curve is the in situ spectrum observed by THEMIS d. The blue and red curves are CRCM spectra. The TWINS-derived BCs significantly improve the agreement with THEMIS (note the log scale). The temperature maps provide global, dynamic, event-specific observations that can make a positive difference in the performance of global models.

Buzulukova et al. (2018) used a combination of modeling and data (both imaging and in situ) to understand system-level dynamic linkages between the magnetosphere and ionosphere during the 14 November 2012 storm (peak Dst −108 nT). RBSP A measured several steep decreases ("dropouts") in particle flux over a broad range (0.1 – 500 keV) of energy (Figure 13a). Dixon et al. (2015) had used multipoint observations by the Van Allen Probes and LANL spacecraft to determine that the 14 November dropouts were caused by motion of the open-closed boundary in the magnetotail. In tandem with two of these dropouts, TWINS observed strong modulation of particle precipitation, as measured by the LAE signal (Figure 13b). To understand this connection, this new study compared field-aligned currents (FACs) from Active Magnetosphere and Planetary Electrodynamics Response Experiment (AMPERE) (Anderson et al., 2008) with those derived from the coupled Block-Adaptive-Tree-Solarwind-Roe-Upwind-Scheme (BATSRUS)-CRCM model. The BATSRUS model uses magnetohydrodynamic assumptions to simulate the outer magnetosphere. Coupling to CRCM improves
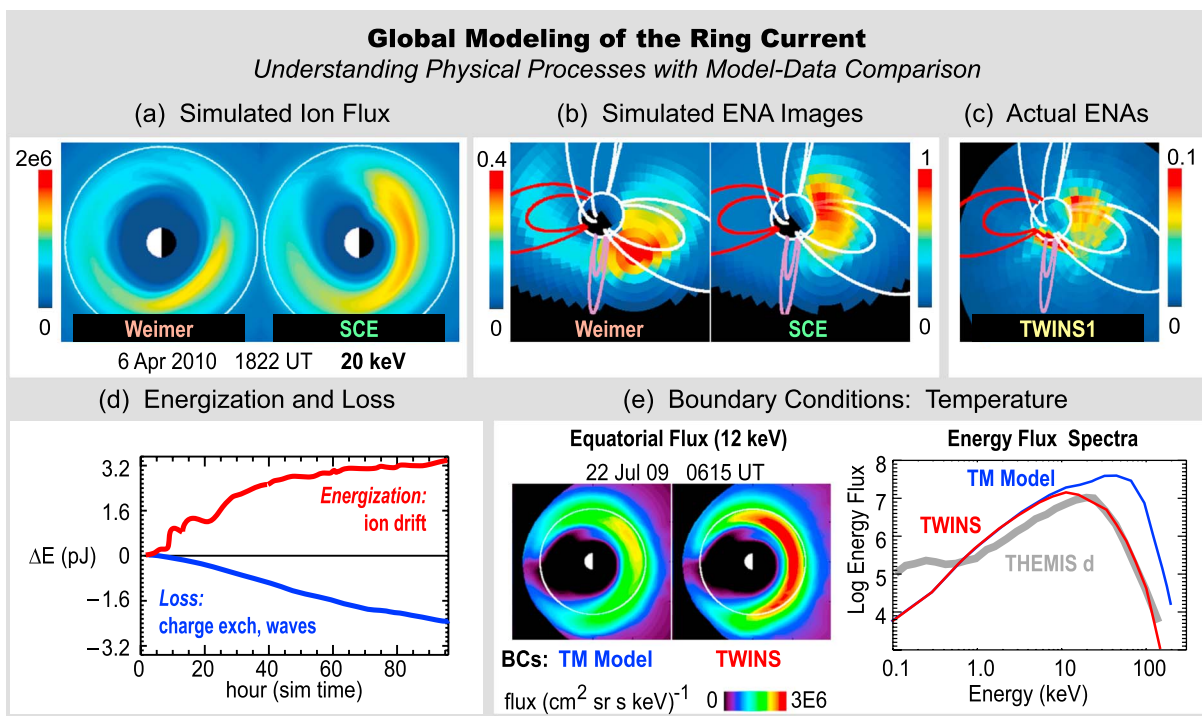
Figure 12. Physical processes of the ring current. Comparison of global models and images help advance understanding and improve the models (Elfritz et al., 2014; Fok et al., 2014). (a) Equatorial 2-D flux maps from two CIMI simulation runs: Weimer E field versus the self-consistent E field (SCE). SCE version correctly puts ring current peak in postmidnight MLT. (b) Simulated ENA images corresponding to the flux maps from Figure 12a. (c) TWINS 1 image (6 April 2010, 1822 UT), with postmidnight peak. (d) Cumulative energy gain or loss from ion drift, charge exchange, and wave scattering. (e) Using TWINS temperatures to specify boundary conditions improves CRCM performance (cf. text). Left: equatorial flux. Right: energy flux spectrum, compared to THEMIS d.

the solutions in the ring current region where the fluid approximation is inadequate. Both the model and measured FACs showed intensifications of the region 2 currents after the dropouts. The new result by Buzulukova et al. (2018) confirmed that the dropouts were caused by the open-closed boundary motion in the tail. Moreover, the TWINS-BATSRUS-CRCM-AMPERE comparison established that the dropouts were a locally observed manifestation of a system-level effect coupling together plasmas in the magnetotail and the ionosphere.

The importance of model-supported interpretation continues to be demonstrated for studies of ion composition and temperature. The BATSRUS and BATSRUS-CRCM global models have helped to show that O^+ concentration can affect the strength of the ring current (Glocer et al., 2013) and that the predominant pathway for O^+ loss may be plasmoids transporting these ions down the magnetotail (Ilie, Skoug, Valek, et al., 2013). Keesee, Elfritz, et al. (2014) used CRCM runs to interpret the results of their superposed epoch analysis of TWINS temperature maps. They found that the convection strength controls the regional ion temperature. Stronger convection brings hotter ions closer to the Earth, leading to higher temperatures.

Understanding the dynamics of big storms is also aided by the use of models. Perez et al. (2016) used the CIMI and Tsyganenko (Tsyganenko & Sitnov, 2005) models to show that the ion PA anisotropy observed by both TWINS and RBSP A on 17 March 2015 is consistent with pitch-angle-dependent drift in a nondipolar field. They found that the outer RC peak (peak 2, Figure 5a) favored parallel anisotropy, because the highly distorted storm time field created a magnetic minimum (with closed drift paths) into which perpendicular ions did not have access. For this same storm, Goldstein et al. (2017) used models to separate space and time effects in THEMIS-observed magnetopause and bow shock crossings, and definitively establish the arrival of the solar wind conditions that caused the storm. They used a model of the plasmapause to interpret Van Allen Probes data and capture the onset of convection in the inner magnetosphere and the first ring current injection of the storm.

Models are essential to interpreting how the complexities of ion-neutral interactions produce the low-altitude ENA signal that TWINS observes. LLera et al. (2017) used an analytical approximation to a full transport code
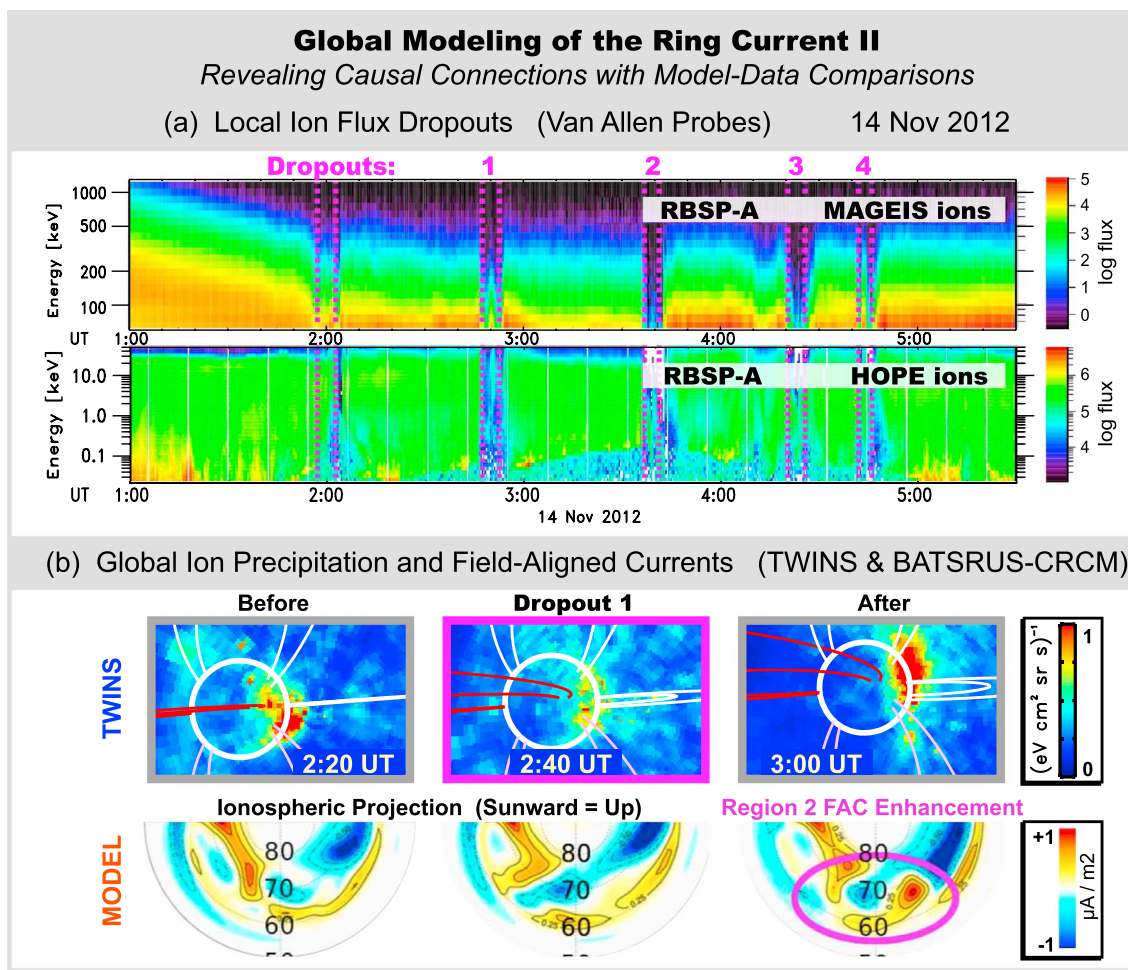
Figure 13. Causal connections in the ring current. TWINS model-data comparisons reveal dynamic linkages between ions and currents, and between different regions of the magnetosphere (Buzulukova et al., 2018). (a) Flux dropouts across 0.1–500 keV measured by RBSP A probe of the Van Allen Probes mission. (b) Top row: TWINS-observed strong modulation of low-altitude emissions during dropout 1. Bottom row: BATSRUS-CRCM field-aligned currents (FACs) intensified after the dropout. AMPERE measurements confirm the model FACs. The model confirms dropouts caused by motions of the open-closed boundary.

to understand the energy loss experienced by ions and neutrals undergoing multiple charge-exchanging interactions to produce LAEs. With the help of the model, they found that the divergent dipole magnetic field line geometry plays a crucial role in helping ENAs to escape to high altitudes. They also found that at altitudes of a few hundred km, ENAs poleward directed ballistic trajectories experience less energy loss than equatorward moving ENAs. Goldstein et al. (2016) ran a Monte Carlo simulation to model the pitch angle distributions of ENAs emerging from low altitudes. They found an energy dependence to the width of particle PADs. More energetic particles have a shorter mean free path for charge-exchanging collisions, and thus have broader PADs than less energetic particles. These results were used to constrain an empirical model of the viewing geometry effect for LAEs.

These recent papers help explain linkages between different regions of the magnetosphere and ionosphere, and reveal some of the important physical mechanisms controlling system-level RC dynamics. M-I coupling can provide feedback that controls the global ring current distribution and evolution. Convection exerts a strong influence on regional heating and cooling of ions. Distortions of the geomagnetic field can modulate mesoscale features of ion flux and pitch angle distributions. Heavy ion enrichment can exert a profound influence on storm time dynamics. More broadly, comparative studies using images alongside global models are an integral part of advancing our understanding of the system-level dynamics of geospace.
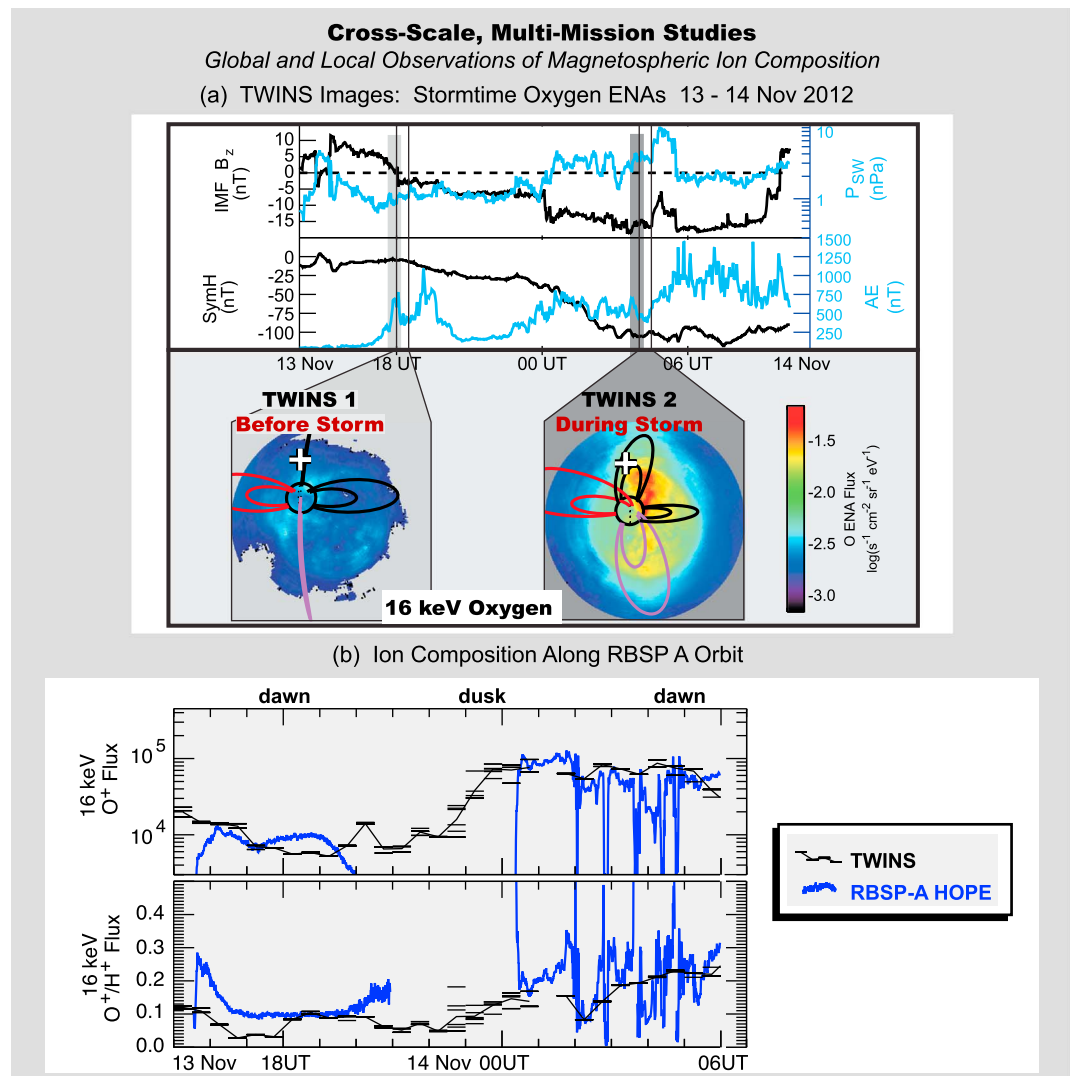
Figure 14. Multiscale observations of ion composition. Imaging plus in situ sampling by the Van Allen Probes (RBSP) reveals both global and local-scale structure (Valek et al., 2015). (a) Energetic neutral atom (ENA) images of storm time oxygen ENAs taken before and during the 14 November 2012 storm indicate a dramatic global increase in O$^+$. (b) Ion composition along the orbit of RBSP A, showing the same strong global spatial and storm phase dependence in both TWINS ENA-derived data (black) and RBSP A in situ data (blue). The local measurements show that regions of enhancement are composed of islands of finer-scale structure.

2.7. Cross-Scale, Multimission Studies

Combining geospace imaging and in situ data permits the study of phenomena and processes that involve multiple spatial scales, from global to local. Almost every published TWINS study has employed data from other missions, including Advanced Composition Explorer (ACE), Akebono, AMPERE, Apollo 16, Cluster, Geotail, Geostationary Operational Environmental Satellite (GOES), Interstellar Boundary Explorer (IBEX), LANL, Meteorological Operational (MetOp) satellites, NOAA, Van Allen Probes, Solar Dynamics Observatory (SDO), Solar and Heliospheric Observatory (SOHO), THEMIS, Thermosphere, Ionosphere, Mesosphere Energetics and Dynamics (TIMED), Upper Atmosphere Research Satellite (UARS), and Wind. During the IMAGE era, there were few attempts at validating the ENA inversion techniques (Keesee et al., 2008; Scime et al., 2002; Vallat et al., 2004; Zhang et al., 2005). In contrast, the majority (over 60%) of TWINS studies involve cross comparison of ENA-derived ion flux with in situ observations. Many of the results already discussed in this review paper use cross-scale comparisons to explore both the very local and more global aspects of inner magnetospheric phenomena (e.g., Elfritz et al., 2014; Goldstein et al., 2016; Katus et al., 2017; Keesee, Chen, et al., 2014; Perez et al., 2015, 2016).
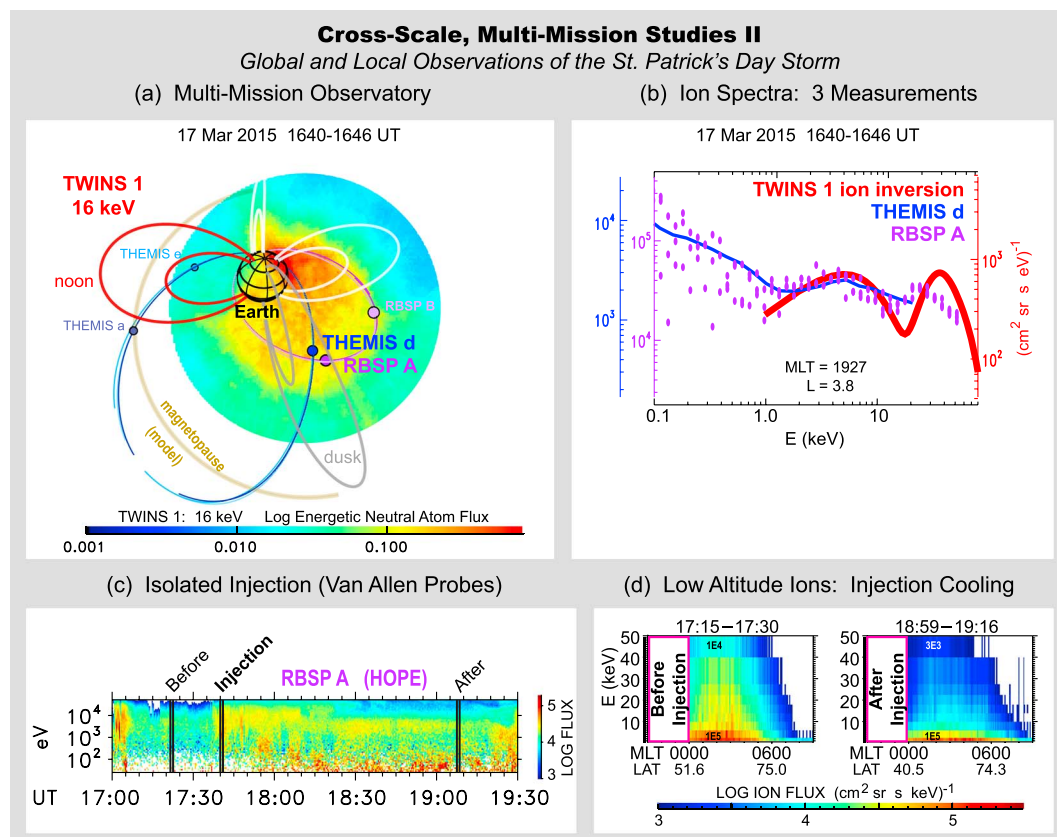
Figure 15. Cross-scale observations of a major storm. Imaging by TWINS, plus multipoint in situ observations by the Van Allen Probes (RBSP), reveals global-to-local-scale structure and causal connections (Goldstein et al., 2017). (a) Multimission conjunction during main phase of 17 March 2015 storm. Mapped onto TWINS 16 keV image are the orbits of three THEMIS and two RBSP spacecraft, and the Shue et al. (1997) model magnetopause. At 1640–1646 UT, THEMIS d and RBSP A were approximately colocated. (b) The three simultaneous ion spectra near [L = 3.8, 1927 MLT] by TWINS 1, THEMIS d, and RBSP A have multiple spectral peaks—a global feature at this time. (c) RBSP A data showing the 1740 UT isolated injection as a doubling of flux in the 1–10 keV range. (d) Energy versus MLT spectrograms of TWINS ion precipitation before and after the isolated RC injection, showing a global change to lower-energy spectra.

Valek et al. (2015) used both TWINS and Van Allen Probes data in the first joint in situ and global observational study of the medium-energy oxygen and hydrogen in the inner magnetosphere. Figure 14a shows TWINS 1 and 2 16 keV oxygen images from before and during the storm of 14 November 2012. There was a dramatic global increase in O^+ during the storm main phase. The species-separated images from the entire event were used to derive TWINS O^+ flux and O^+/H^+ flux ratios along the RBSP A orbit. These are compared with corresponding data from RBSP A in Figure 14b. The two measurements give complementary views of two different spatial scales. RBSP A provides a detailed in situ measurement, and TWINS captures a global view at lower spatial resolution. The fact that the large-scale spatial and temporal dependencies are in good agreement validates the global oxygen imaging technique, enabling confident system-level interpretation. For example, Valek et al. (2015) concluded that O^+ ions were concentrated close to the magnetic equator (i.e., at large pitch angles). The comparison also reveals global-to-local relationships: the RBSP A data indicate that the larger-scale regions of O^+ enhancement are actually composed of multiple islands of finer-scale structure.

Goldstein et al. (2017) analyzed cross-scale observations of the 17 March 2015 storm, by THEMIS, Van Allen Probes, and TWINS, plus upstream solar wind conditions by Advanced Composition Explorer and Wind. Utilization of multiple observatories enabled tracking the progress of the event, from its commencement at the dayside bow shock and magnetopause to the inner magnetosphere during the storm's main phase. Dayside boundary motions were observed by the three THEMIS spacecraft and interpreted via empirical boundary models. Van Allen Probes captured the onset of global magnetospheric convection (cf. section 1.1.1) and its

effects on the plasmasphere and RC, including a wide variety of spatial/spectral ion structures. The main phase TWINS images show how local structures compose regions of enhanced RC pressure.

Figure 15a shows a close conjunction of the three missions during 1640–1646 UT, when RBSP A and THEMIS d were approximately colocated inside the peak of the partial RC. Figure 15b plots a three-way comparison of ion flux spectra. The two peaks in the TWINS ion spectrum (obtained via inversion; cf. section 2.1) were also measured by RBSP A and are consistent with THEMIS within its energy range. According to the TWINS inversions these spectral peaks were a global feature. Later in the storm, an isolated injection was observed by RBSP A at 1740 UT (Figure 15c). This injection brought in fresh ions with lower-average energies, which led to a global change to less energetic spectra in precipitating ions (Figure 15d), but increased the total pressure in the trapped ions.

Cross-scale measurements of the storm time ring current exhibit an enormous degree of structure—spatial, spectral, and temporal—implying that plasma transport during storms is made up of many individual bursts and microinjections. Multiobservatory measurements that encompass all these scales obtain a much more comprehensive view of geospace dynamics than any one observation alone.

3. Conclusion

The ring current has been studied for decades (Singer, 1957), and its global evolution was extensively measured and analyzed by the IMAGE mission (Burch, 2005). What have we learned from TWINS?

1. Stereo ENA imaging has revealed extra dimensionality and structure that was previously undetected by monoscopic imaging (Goldstein et al., 2012a; Perez et al., 2015).
2. Continuous coverage by two imagers has allowed the monitoring of storms from start to finish (e.g., Perez et al., 2012), without the gaps in coverage experienced by IMAGE, for example.
3. The development of a method to deconvolve the optically thick low-altitude ENA signal has extended ENA analysis capabilities, and increased the range of geomagnetic conditions for which inversions can be performed (Bazell et al., 2010; Goldstein et al., 2013, 2016).
4. ENA-based temperature analysis has been greatly refined and validated, and has been applied to an unprecedented sequence of solar activity changes in SC 23 and SC 24 (Keesee, Chen, et al., 2014; Keesee, Elfritz, et al., 2014).
5. ENA-based ion composition (H^+, O^+) analysis has been applied to modern storms, for a significantly wider range of energy (Valek et al., 2015, 2018).
6. Geocoronal imaging has revealed a surprising amount of time variability and structure in the neutral H exosphere that is driven by both Sun and solar wind (Bailey & Gruntman, 2013; Zoennchen et al., 2015, 2017).
7. Global models have been measurably improved (e.g., Elfritz et al., 2014; Fok et al., 2010, 2014).
8. Multimission studies that include ENA imaging have made essential contributions to our understanding of the cross-scale physics of storms and substorms (e.g., Goldstein et al., 2017; Valek et al., 2015).

The extraordinary and fortuitous wealth of simultaneous in situ measurements available to complement TWINS global imaging has fostered huge leaps forward in cross-scale studies of the inner magnetosphere (section 2.7). These multipoint, multiscale, multimission observations have provided a uniquely valuable and comprehensive window into the geospace response.

The TWINS mission of opportunity was designed and planned to last for 2 years from June 2008, when it started delivering simultaneous stereo imaging of the Earth's magnetosphere. The mission provided these data through the fall of 2016, when TWINS 2 suffered an actuator and/or electronics failure that precludes this instrument from returning useful data. The ENA sensor and LAD on TWINS 1 continue to operate well and return high-quality data to support TWINS mission science, although with single-perspective viewing going forward.

What does the future hold for geospace ENA and geocoronal imaging? We conclude this review by briefly discussing a few possible next steps.

1. *Fine structure of the ring current.* A major scientific theme of this review has been that global or mesoscale features in images are composed of multiple islands of fine-scale structures. Stereo inversions have revealed more structure than monoscopic imaging. However, there is still much more structure in the local measurements (e.g., Goldstein et al., 2017; Kistler et al., 1989). An obvious next step for ENA science is to understand

how much of this local structure can theoretically be measured by a LOS-integrated measurement. A systematic determination of the intrinsic minimum spatial resolution obtainable for geospace ENA imaging has yet to be performed. This information could motivate the development of an imager with improved resolution to measure finer-scale structure.

2. *M-I coupling.* Another major theme of this review has been the importance of M-I coupling in governing the dynamics of multiple geospace plasmas, including the ring current. A main mechanism for this coupling is provided by the region 2 FACs that link the ring current and ionosphere (Iijima & Potemra, 1976). A study by Brandt et al. (2005) used IMAGE High-Energy Neutral Atom ion pressure distributions to compute these region 2 FACs. Work is underway to reproduce this capability for TWINS data (Wood et al., 2015). Electrodynamic coupling is a central science target of the Magnetosphere Energetics, Dynamics, and Ionospheric Coupling Mission mission concept (NRC Heliophysics Decadal Survey, 2012).

3. *Ion precipitation and ion-neutral interactions.* A second main M-I coupling mechanism is ion precipitation, which TWINS results have shown is a joint process between the spiraling ions and the low-altitude neutral exosphere. TWINS has made important advances in understanding and quantifying this complicated phenomenon, but significant work is still required before LAE interpretation is as robust as deconvolution of the trapped ion population. The biggest remaining challenge is a reliable means of factoring out the strong viewing geometry effect caused by the highly directional LAE signal (Bazell et al., 2010; Goldstein et al., 2016; Pollock et al., 2009; Roelof & Skinner, 2000). Higher-resolution imaging is essential to reduce the uncertainty in LAE deconvolutions.

4. *Exospheric science.* TWINS has made essential progress in characterizing the spatial asymmetry and time variation of the neutral H exosphere. Recent work has also established the importance of this geospace population in governing ring current losses by ENA production (Ilie, Skoug, Funsten, et al., 2013). Because the exospheric density changes measurably on multiple time scales (from one solar cycle to the next, within a solar cycle, and even during storms), existing empirical models may be adequate only for a limited time span. Future progress may require continuous geocoronal monitoring.

5. *Complexity of ENA image interpretation.* ENA images are a two-dimensional convolution of two different, time-dependent populations. The neutral H exosphere varies in three dimensions. Ring current ions have 5 degrees of freedom (three spatial dimensions plus energy and pitch angle). Consequently, interpretation of these images is not simple, and ion inversions are not yet generally trusted or understood to the degree that in situ measurements are. The TWINS mission has partially bridged this gap via multiple validation studies and cross-scale comparisons (section 2.7). However, a remaining challenge is that ENA inversions are typically provided on demand rather than as a routine data product. In the future, budgets should include the resources needed to make inversions and other higher-level science products routinely available.

6. *Next-generation ENA imager.* Previous or existing ENA imagers are large and heavy (Westlake et al., 2016). Imagers capable of measuring ENAs below 10 keV are either 1-D/linear spectrometers like TWINS, or single-pixel cameras like the Interstellar Boundary Explorer (McComas, Allegrini, Bochsler, et al., 2009). To create a 2-D image with this existing technology requires actuation or satellite motion. Development of a small, light, 2-D ENA imager would reduce the resources needed to study space plasmas and upper atmospheres throughout the solar system.

References

Akasofu, S.-I., Chapman, S., & Venkatesan, B. (1963). The main phase of great magnetic storms. *Journal of Geophysical Research*, *68*, 3345–3350. https://doi.org/10.1029/JZ068i011p03345

Anderson, A. D., & Francis, W. E. (1966). The variation of the neutral atmospheric properties with local time and solar activity from 100 to 10,000 km. *Journal of the Atmospheric Sciences*, *23*, 110–124. https://doi.org/10.1175/1520-0469(1966)023<0110:TVOTNA>2.0.CO;2

Anderson, B. J., Korth, H., Waters, C. L., Barnes, R. M., & Weiss, M. B. (2008). The Active Magnetosphere and Planetary Electrodynamics Response Experiment (AMPERE): A new facility for real-time magnetosphere-ionosphere monitoring. *Eos, Transactions American Geophysical Union*. Fall 2008 Meeting Supplement, SA51A-1550.

Angelopoulos, V. (2008). The THEMIS mission. *Space Science Reviews*, *141*, 5. https://doi.org/10.1007/s11214-008-9336-1

Angelopoulos, V., Sibeck, D., Carlson, C. W., McFadden, J. P., Larson, D., Lin, R. P., et al. (2008). First results from the THEMIS mission. *Space Science Reviews*, *141*, 453–476. https://doi.org/10.1007/s11214-008-9378-4

Bailey, J. J., & Gruntman, M. (2011). Experimental study of exospheric hydrogen atom distributions by Lyman-alpha detectors on the TWINS mission. *Journal of Geophysical Research*, *116*, A09302. https://doi.org/10.1029/2011JA016531

Bailey, J. J., & Gruntman, M. (2013). Observations of exosphere variations during geomagnetic storms. *Geophysical Research Letters*, *40*, 1907–1911. https://doi.org/10.1002/grl.50443

Bazell, D., Roelof, E., Sotirelis, T., Brandt, P., Nair, H., Valek, P., et al. (2010). Comparison of TWINS images of low-altitude emission (LAE) of energetic neutral atoms with DMSP precipitating ion fluxes. *Journal of Geophysical Research*, *115*, A10204. https://doi.org/10.1029/2010JA015644

Birn, J., Thomsen, M. F., Borovsky, J. E., Reeves, G. D., McComas, D. J., & Belian, R. D. (1997). Characteristic plasma properties during dispersionless substorm injections at geosynchronous orbit. *Journal of Geophysical Research*, *102*, 2309–2324. https://doi.org/10.1029/96JA02870

Borovsky, J. E. (2014). Feedback of the magnetosphere. *Science*, *343*, 1086–1087. https://doi.org/10.1126/science. 1250590

Borovsky, J. E., & Denton, M. H. (2006). Differences between CME-driven storms and CIR-driven storms. *Journal of Geophysical Research*, *111*, A07S08. https://doi.org/10.1029/2005JA011447

Borovsky, J. E., Thomsen, M. F., & McComas, D. J. (1997). The super-dense plasma sheet: Plasmaspheric origin, solar wind origin, or ionospheric origin? *Journal of Geophysical Research*, *102*, 22,089–22,097.

Bothmer, V., & Daglis, I. A. (2007). *Space weather: Physics and effects*. Berlin, New York: Praxis. https://doi.org/10.1007/978-3-540-34578-7

Brandt, P. C., Barabash, S., Roelof, E. C., & Chase, C. J. (2001a). Energetic neutral atom imaging at low altitudes from the Swedish microsatellite Astrid: Observations at low ($\leq$10 keV) energies. *Journal of Geophysical Research*, *106*, 24,663–24,674. https://doi.org/10.1029/2000JA900119

Brandt, P. C., Barabash, S., Roelof, E. C., & Chase, C. J. (2001b). ENA imaging at low altitudes from the Swedish microsatellite Astrid: Extraction of the equatorial ion distribution. *Journal of Geophysical Research*, *106*(A11), 25,731–25,744.

Brandt, P. C., DeMajistre, R., Roelof, E. C., Ohtani, S., Mitchell, D. G., & Mende, S. B. (2002). Global ENA imaging of the plasmasheet and ring current during substorms. *Journal of Geophysical Research*, *107*(A12), 1454. https://doi.org/10.1029/2002JA009307

Brandt, P. C., Goldstein, J., Anderson, B. J., Korth, H., Immel, T. J., Roelof, E. C., et al. (2005). On the relation between electric fields in the inner magnetosphere, ring current, auroral conductance, and plasmapause motion. In J. L. Burch, M. Schulz, & H. Spence (Eds.), *Inner magnetosphere interactions: New perspectives from imaging* (pp. 159). Washington, DC: American Geophysical Union.

Brandt, P. C., Mitchell, D. G., Ebihara, Y., Sandel, B. R., Roelof, E. C., Burch, J. L., & Demajistre, R. (2002). Global IMAGE/HENA observations of the ring current: Examples of rapid response to IMF and ring current-plasmasphere interaction. *Journal of Geophysical Research*, *107*(A11), 1359. https://doi.org/10.1029/2001JA000084

Brandt, P. C., Ohtani, P. S., Mitchell, D. G., Fok, M.-C., Roelof, E. C., & DeMajistre, R. (2002). Global ENA observations of the storm mainphase ring current: Implications for skewed electric fields in the inner magnetosphere. *Geophysical Research Letters*, *29*(20), 1954. https://doi.org/10.1029/2002GL015160

Burch, J. L. (2003). The first two years of IMAGE. *Space Science Reviews*, *109*, 1–24.

Burch, J. L. (2005). Magnetospheric imaging: Promise to reality. *Reviews of Geophysics*, *43*, RG3001. https://doi.org/10.1029/2004RG000160

Burch, J. L., Mende, S. B., Mitchell, D. G., Moore, T. E., Pollock, C. J., Reinisch, B. W., et al. (2001). Views of Earth's magnetosphere with the IMAGE satellite. *Science*, *291*, 619.

Burlaga, L. F. (1975). Interplanetary streams and their interaction with the Earth. *Space Science Reviews*, *17*, 327–352. https://doi.org/10.1007/BF00718578

Buzulukova, N., Goldstein, J., Fok, M.-C, Glocer, A., Valek, P., McComas, D., et al. (2018). Magnetosphere dynamics during the 14 November 2012 storm inferred from TWINS, AMPERE, Van Allen Probes, and BATS-R-US-CRCM. *Annales Geophysicae*, *36*, 107–124. https://doi.org/10.5194/angeo-36-107-2018

Buzulukova, N., Fok, M.-C., Goldstein, J., Valek, P., McComas, D., & Brandt, P. C. (2010). Ring current dynamics in modest and strong storms: Comparative analysis of TWINS and IMAGE/HENA data with CRCM. *Journal of Geophysical Research*, *115*, A12234. https://doi.org/10.1029/2010JA015292

Buzulukova, N., Fok, M.-C., Roelof, E. C., Redfern, J., Goldstein, J., Valek, P., & McComas, D. J. (2013). Comparative analysis of low altitude ENA emissions in two substorms. *Journal of Geophysical Research: Space Physics*, *118*, 724–731. https://doi.org/10.1002/jgra.50103

Candey, R. M., Bilitza, D., Chimiak, R., Cooper, J. F., Garcia, L. N., Harris, B., et al. (2012). Cross-mission analysis through Space Physics Data Facility (SPDF) services. In *AGU Fall Meeting Abstracts*.

Cane, H. V., & Richardson, I. G. (2003). Interplanetary coronal mass ejections in the near-Earth solar wind during 1996–2002. *Journal of Geophysical Research*, *108*(A4), 1156. https://doi.org/10.1029/2002JA009817

Chapman, S. (1931). The absorption and dissociative or ionizing effect of monochromatic radiation in an atmosphere on a rotating Earth. *Proceedings of the Physical Society*, *43*, 26–45. https://doi.org/10.1088/0959-5309/43/1/305

Daglis, I. A., Sarris, E. T., & Wilken, B. (1993). AMPTE/CCE CHEM observations of the energetic ion population at geosynchronous altitudes. *Annales Geophysicae*, *11*, 685–696.

Daglis, I. A., Thorne, R. M., Baumjohann, W., & Orsini, S. (1999). The terrestrial ring current: Origin, formation, and decay. *Reviews of Geophysics*, *37*, 407–438.

Dalgarno, A. (1962). Range and energy loss. In D. R. Bates (Ed.), *Atomic and molecular processes* (623 pp.). New York: Academic Press.

Dalgarno, A., & Griffing, G. W. (1958). Energy per ion pair for electron and proton beams in atomic hydrogen. *Proceedings of the Royal Society of London. Series A*, *248*, 415–428. https://doi.org/10.1098/rspa.1958.0253

Delmonico, E. (2015). *Extending TWINS composition analysis of oxygen and hydrogen*. San Antonio, TX: University of Texas at San Antonio.

Denton, M. H., Jordanova, V. K., Henderson, M. G., Skoug, R. M., Thomsen, M. F., Pollock, C. J., et al. (2005). Storm-time plasma signatures observed by IMAGE/MENA and comparison with a global physics-based model. *Geophysical Research Letters*, *32*, L17102. https://doi.org/10.1029/2005GL023353

Dessler, A. J., & Parker, E. N. (1959). Hydromagnetic theory of geomagnetic storms. *Journal of Geophysical Research*, *64*, 2239–2252. https://doi.org/10.1029/JZ064i012p02239

Dixon, P., MacDonald, E. A., Funsten, H. O., Glocer, A., Grande, M., Kletzing, C., et al. (2015). Multipoint observations of the open-closed field line boundary as observed by the Van Allen Probes and geostationary satellites during the 14 November 2012 geomagnetic storm. *Journal of Geophysical Research: Space Physics*, *120*, 6596–6613. https://doi.org/10.1002/2014JA020883

Dryer, M., Smith, Z. K., Smith, E. J., Mihalov, J. D., Wolfe, J. H., Steinolfson, R. S., & Wu, S. T. (1978). Dynamic MHD modeling of solar wind corotating stream interaction regions observed by Pioneer 10 and 11. *Journal of Geophysical Research*, *83*, 4347–4352. https://doi.org/10.1029/JA083iA09p04347

Dungey, J. W. (1961). Interplanetary magnetic field and the auroral zones. *Physical Review Letters*, *6*, 47–48.

Ebihara, Y., Ejiri, M., Nilsson, H., Sandahl, I., Grande, M., Fennell, J., et al. (2004). Multiple discrete-energy ion features in the inner magnetosphere: 9 February 1998, event. *Annales Geophysicae*, *22*, 1297. https://doi.org/10.5194/angeo-22-1297-2004

Elfritz, J. G., Keesee, A. M., Buzulukova, N., Fok, M. C., & Scime, E. E. (2014). First results using TWINS-derived ion temperature boundary conditions in CRCM. *Journal of Geophysical Research: Space Physics*, *119*, 3345–3361. https://doi.org/10.1029/2013JA019555

Fisk, L. A., & Lee, M. A. (1980). Shock acceleration of energetic particles in corotating interaction regions in the solar wind. *The Astrophysical Journal*, *237*, 620. https://doi.org/10.1086/157907

Fok, M., Wolf, R. A., Spiro, R. W., & Moore, T. E. (2001). Comprehensive computational model of Earth's ring current. *Journal of Geophysical Research*, *106*, 8417–8424.

Fok, M.-C., Buzulukova, N., Chen, S.-H., Valek, P. W., Goldstein, J., & McComas, D. J. (2010). Simulation and TWINS observations of the 22 July 2009 storm. *Journal of Geophysical Research*, *115*, A12231. https://doi.org/2010JA015443

Fok, M.-C., Buzulukova, N. Y., Chen, S.-H., Glocer, A., Nagai, T., Valek, P., & Perez, J. D. (2014). The comprehensive inner magnetosphere-ionosphere model. *Journal of Geophysical Research: Space Physics*, *119*, 7522–7540. https://doi.org/10.1002/2014JA020239

Fok, M.-C., Kozyra, J. U., Nagy, A. F., & Cravens, T. E. (1991). Lifetime of ring current particles due to Coulomb collisions in the plasmasphere. *Journal of Geophysical Research*, *96*, 7861–7867. https://doi.org/10.1029/90JA02620

Fok, M.-C., Moore, T. E., Wilson, G. R., Perez, J. D., Zhang, X., Brandt, P. C., et al. (2003). Global ENA IMAGE simulations. *Space Science Reviews*, *109*, 77–103.

Garcia, H. A., & Spjeldvik, W. N. (1985). Anisotropy characteristics of geomagnetically trapped ions. *Journal of Geophysical Research*, *90*, 347–358. https://doi.org/10.1029/JA090iA01p00347

Gary, S. P., Thomsen, M. F., Yin, L., & Winske, D. (1995). Electromagnetic proton cyclotron instability: Interactions with magnetospheric protons. *Journal of Geophysical Research*, *100*(A11), 21,961–21,972.

Glocer, A., Fok, M.-C., Meng, X., Toth, G., Buzulukova, N., Chen, S.-H., & Lin, K. (2013). CRCM + BATS-R-US two-way coupling. *Journal of Geophysical Research: Space Physics*, *118*, 1635–1650. https://doi.org/10.1002/jgra.50221

Glocer, A., Fok, M.-C., Nagai, T., Toth, G., Guild, T., & Blake, J. (2011). Rapid rebuilding of the outer radiation belt. *Journal of Geophysical Research*, *116*, A09213. https://doi.org/10.1029/2011JA016516

Gold, T. (1959). Motions in the magnetosphere of the Earth. *Journal of Geophysical Research*, *64*, 1219–1224. https://doi.org/10.1029/JZ064i009p01219

Goldstein, J. (2006). Plasmasphere response: Tutorial and review of recent imaging results. *Space Science Reviews*, *124*, 203–216. https://doi.org/10.1007/s11214-006-9105-y

Goldstein, J., & McComas, D. J. (2013). Five years of stereo magnetospheric imaging by TWINS. *Space Science Reviews*, *180*, 39–70. https://doi.org/10.1007/s11214-013-0012-8

Goldstein, J., Angelopoulos, V., Pascuale, S. D., Funsten, H. O., Kurth, W. S., LLera, K., et al. (2017). Cross-scale observations of the 2015 St. Patrick's day storm: THEMIS, Van Allen Probes, and TWINS. *Journal of Geophysical Research: Space Physics*, *122*, 368–392. https://doi.org/10.1002/2016JA023173

Goldstein, J., Bisikalo, D. V., Shematovich, V. I., Gérard, J.-C., Søraas, F., McComas, D. J., et al. (2016). Analytical estimate for low-altitude ENA emissivity. *Journal of Geophysical Research: Space Physics*, *121*, 1167–1191. https://doi.org/10.1002/2015JA021773

Goldstein, J., Valek, P., McComas, D. J., & Redfern, J. (2012a). TWINS energetic neutral atom observations of local-time-dependent ring current anisotropy. *Journal of Geophysical Research*, *117*, A11213. https://doi.org/10.1029/2012JA017804

Goldstein, J., Valek, P., McComas, D. J., & Redfern, J. (2012b). Latitudinal anisotropy in ring current energetic neutral atoms. *Geophysical Research Letters*, *39*, L08102. https://doi.org/10.1029/2012GL051417

Goldstein, J., Valek, P., McComas, D. J., Redfern, J., & Soraas, F. (2013). Local-time-dependent low-altitude ion spectra deduced from TWINS ENA images. *Journal of Geophysical Research: Space Physics*, *118*, 2928–2950. https://doi.org/10.1002/jgra.50222

Gosling, J. T. (1993). The solar flare myth. *Journal of Geophysical Research*, *98*, 18,937–18,949. https://doi.org/10.1029/93JA01896

Gosling, J. T., Hildner, E., MacQueen, R. M., Munro, R. H., Poland, A. I., & Ross, C. L. (1974). Mass ejections from the Sun: A view from Skylab. *Journal of Geophysical Research*, *79*, 4581–4587. https://doi.org/10.1029/JA079i031p04581

Grimes, E. W., Perez, J. D., Goldstein, J., McComas, D. J., & Valek, P. (2010). Global observations of ring current dynamics during CIR-driven geomagnetic storms in 2008. *Journal of Geophysical Research*, *115*, A11207. https://doi.org/10.1029/2010JA015409

Grimes, E. W., Perez, J. D., Goldstein, J., McComas, D. J., Valek, P., & Turner, D. (2013). Comparison of TWINS and THEMIS observations of proton pitch angle distributions in the ring current during the 29 May 2010 geomagnetic storm. *Journal of Geophysical Research: Space Physics*, *118*, 4895–4905. https://doi.org/10.1002/jgra.50455

Hamilton, D. C., Gloeckler, G., Ipavich, F. M., Wilken, B., & Stuedemann, W. (1988). Ring current development during the great geomagnetic storm of February 1986. *Journal of Geophysical Research*, *93*, 14,343–14,355. https://doi.org/10.1029/JA093iA12p14343

Henderson, M. G., Reeves, G. D., Spence, H. E., Sheldon, R. B., Jorgensen, A. M., Blake, J. B., & Fennell, J. F. (1997). First energetic neutral atom images from Polar. *Geophysical Research Letters*, *24*, 1167–1170. https://doi.org/10.1029/97GL01162

Hodges, R. R. (1994). Monte Carlo simulation of the terrestrial hydrogen exosphere. *Journal of Geophysical Research*, *99*, 23,229–23,247.

Iijima, T., & Potemra, T. A. (1976). The amplitude distribution of field-aligned currents at northern high latitudes observed by TRIAD. *Journal of Geophysical Research*, *81*(13), 2165–2174.

Ilie, R., Skoug, R. M., Funsten, H. O., Liemohn, M. W., Bailey, J. J., & Gruntman, M. (2013). The impact of geocoronal density on ring current development. *Journal of Atmospheric and Solar-Terrestrial Physics*, *99*, 92–103. https://doi.org/10.1016/j.jastp.2012.03.010

Ilie, R., Skoug, R. M., Valek, P., Funsten, H. O., & Glocer, A. (2013). Global view of inner magnetosphere composition during storm time. *Journal of Geophysical Research: Space Physics*, *118*, 7074–7084. https://doi.org/10.1002/2012JA018468

Kamide, Y., Yokoyama, N., Gonzalez, W., Tsurutani, B. T., Daglis, I. A., Brekke, A., & Masuda, S. (1998). Two-step development of geomagnetic storms. *Journal of Geophysical Research*, *103*, 6917–6922. https://doi.org/10.1029/97JA03337

Katus, R. M., Keesee, A. M., Scime, E., & Liemohn, M. W. (2017). Storm time equatorial magnetospheric ion temperature derived from TWINS ENA flux. *Journal of Geophysical Research: Space Physics*, *122*, 3985–3996. https://doi.org/10.1002/2016JA023824

Keesee, A., Buzulukova, N., Goldstein, J., McComas, D. J., Scime, E. E., Spence, H., & Tallaksen, K. (2011). Remote observations of ion temperatures in the quiet time magnetosphere. *Geophysical Research Letters*, *38*, L03104. https://doi.org/10.1029/2010GL045987

Keesee, A. M. (2017). A review of dawn-dusk asymmetries observed using the TWINS mission of opportunity. In S. Haaland, A. Runov, & C. Forsyth (Eds.), *Dawn-dusk asymmetries in planetary plasma environments, Geophysical Monograph* (Vol. 229). Washington, DC: American Geophysical Union. https://doi.org/10.1001/9781119216346

Keesee, A. M., & Scime, E. E. (2015). Database of ion temperature maps during geomagnetic storms. *Earth and Space Science*, *2*, 39–46. https://doi.org/10.1002/2014EA000061

Keesee, A. M., Chen, M. W., Scime, E. E., & Lui, A. T. Y. (2014). Regions of ion energization observed during the Galaxy-15 substorm with TWINS. *Journal of Geophysical Research: Space Physics*, *119*, 8274–8287. https://doi.org/10.1002/2014JA020466

Keesee, A. M., Elfritz, J. G., Fok, M.-C., McComas, D., & Scime, E. (2014). Superposed epoch analysis of ion temperature evolution during CME- and CIR/HSS-driven storms. *Journal of Atmospheric and Solar-Terrestrial Physics*, *115*, 67–78. https://doi.org/10.1016/j.jastp.2013.08.009

Keesee, A. M., Elfritz, J. G., McComas, D. J., & Scime, E. E. (2012). Inner magnetosphere convection and magnetotail structure of hot ions imaged by ENA during a HSS-driven storm. *Journal of Geophysical Research*, *117*, A00L06. https://doi.org/10.1029/2011JA017319

Keesee, A. M., Katus, R. M., & Scime, E. E. (2017). The effect of storm driver and intensity on magnetospheric ion temperatures. *Journal of Geophysical Research: Space Physics*, *122*, 9414–9426. https://doi.org/10.1002/2017JA023973

Keesee, A. M., Scime, E., & Moldwin, M. B. (2008). Remote measurements of ion temperatures in the terrestrial magnetotail. *Journal of Geophysical Research*, 113, A00A03. https://doi.org/10.1029/2008JA013130

Kistler, L. M., Ipavich, F. M., Hamilton, D. C., Gloeckler, G., Wilken, B., Kremser, G., & Studemann, W. (1989). Energy spectra of the major ion species in the ring current during geomagnetic storms. *Journal of Geophysical Research*, 94(A4), 3579–3599.

Li, X., Baker, D. N., Temerin, M., Peterson, W. K., & Fennell, J. F. (2000). Multiple discrete-energy ion features in the inner magnetosphere: Observations and simulations. *Geophysical Research Letters*, 27, 1447–1450. https://doi.org/10.1029/1999GL010745

LLera, K. (2017). Energetics of near-earth particles: Energy correction in observation and measurement (PhD thesis). University of Texas San Antonio.

LLera, K., Goldstein, J., McComas, D., & Valek, P. (2017). Low altitude emission of energetic neutral atoms: Multiple interactions and energy loss. *Journal of Geophysical Research: Space Physics*, 122, 10,203–10,234. https://doi.org/10.1002/2017JA024016

LLera, K., Goldstein, J., Redfern, J. A., Valek, P. W., & McComas, D. J. (2012). Statistical correlation of TWINS low-altitude emission with stormtime solar wind pressure and Sym-H. In *Eos, Transactions American Geophysical Union*. Fall 2012 Meeting Supplement, SM41A-2184.

Lotko, W. (2013). Coupling and feedback in the stormtime magnetosphere-ionosphere-thermosphere interaction (invited). In *AGU Fall Meeting Abstracts*.

Lui, A. T. Y., Brandt, P. C., & Mitchell, D. G. (2005). Observations of energetic neutral oxygen by IMAGE/HENA and Geotail/EPIC. *Geophysical Research Letters*, 32, L13104. https://doi.org/10.1029/2005GL022851

Lui, A. T. Y., McEntire, R. W., & Krimigis, S. M. (1987). Evolution of the ring current during two geomagnetic storms. *Journal of Geophysical Research*, 92, 7459–7470. https://doi.org/10.1029/JA092iA07p07459

Lui, A. T. Y., McEntire, R. W., Sibeck, D. G., & Krimigis, S. M. (1990). Recent findings on angular distributions of dayside ring current energetic ions. *Journal of Geophysical Research*, 95, 20,839–20,851. https://doi.org/10.1029/JA095iA12p20839

Ma, S.-Y., Yan, W.-N., & Xu, L. (2015). Tomographic reconstruction of storm time RC ion distribution from ENA images on board multiple spacecraft. *Journal of Geophysical Research: Space Physics*, 120, 9334–9354. https://doi.org/10.1002/2015JA021601

Mauk, B. H., Fox, N. J., Kanekal, S. G., Kessel, R. L., Sibeck, D. G., & Ukhorskiy, A. (2013). Science objectives and rationale for the radiation belt storm probes mission. *Space Science Reviews*, 179, 3–27. https://doi.org/10.1007/s11214-012-9908-y

McComas, D. J., Bame, S. J., Barraclough, B. L., Donart, J. R., Elphic, R. C., Gosling, J. T., et al. (1993). Magnetospheric Plasma Analyzer (MPA): Initial three-spacecraft observations from geosynchronous orbit. *Journal of Geophysical Research*, 98, 13,453–13,465. https://doi.org/10.1029/93JA00726

McComas, D. J., Allegrini, F., Baldonado, J., Blake, B., Brandt, P., Burch, J., et al. (2009). The Two Wide-angle Imaging Neutral-atom Spectrometers (TWINS) NASA mission-of-opportunity. *Space Science Reviews*, 142, 157–231. https://doi.org/10.1007/s11214-008-9467-4

McComas, D. J., Allegrini, F., Bochsler, P., Bzowski, M., Christian, E. R., Crew, G. B., et al. (2009). Global observations of the interstellar interaction from the interstellar boundary explorer (IBEX). *Science*, 326, 959–962. https://doi.org/10.1126/science.1180906

McComas, D. J., Buzulukova, N., Connors, M. G., Dayeh, M. A., Goldstein, J., Funsten, H. O., et al. (2012). Two Wide-angle Imaging Neutral-atom Spectrometers and interstellar boundary explorer energetic neutral atom imaging of the 5 April 2010 substorm. *Journal of Geophysical Research*, 117, A03225. https://doi.org/10.1029/2011JA017273

Mitchell, D. G., Brandt, P. C., Roelof, E. C., Hamilton, D. C., Retterer, K. C., & Mende, S. (2003). Global imaging of O+ from IMAGE/HENA. *Space Science Reviews*, 109, 63–75. https://doi.org/10.1023/B:SPAC.0000007513.55076.00

Nass, H. U., Zoennchen, J. H., Lay, G., & Fahr, H. J. (2006). The TWINS-LAD mission: Observations of terrestrial Lyman-α fluxes. *Astrophysics and Space Sciences Transactions*, 2, 27–31.

NRC Heliophysics Decadal Survey (2012). *Solar and space physics: A science for a technological society*. Washington, DC: National Academies Press.

Østgaard, N., Mende, S. B., Frey, H. U., Frank, L. A., & Sigwarth, J. B. (2003). Observations of non-conjugate theta aurora. *Geophysical Research Letters*, 30(21), 2125. https://doi.org/10.1029/2003GL017914

Perez, J. D., Grimes, E. W., Goldstein, J., McComas, D. J., Valek, P., & Billor, N. (2012). Evolution of CIR storm on 22 July 2009. *Journal of Geophysical Research*, 117, A09221. https://doi.org/10.1029/2012JA017572

Perez, J. D., Goldstein, J., McComas, D. J., Valek, P., Buzulukova, N., Fok, M.-C., & Singer, H. J. (2015). TWINS stereoscopic imaging of multiple peaks in the ring current. *Journal of Geophysical Research: Space Physics*, 120, 368–383. https://doi.org/10.1002/2014JA020662

Perez, J. D., Goldstein, J., McComas, D. J., Valek, P., Fok, M.-C., & Hwang, K.-J. (2016). Global images of trapped ring current ions during main phase of 17 March 2015 geomagnetic storm as observed by TWINS. *Journal of Geophysical Research: Space Physics*, 121, 6509–6525. https://doi.org/10.1002/2016JA022375

Perez, J. D., Kozlowski, G., Brandt, P. C., Mitchell, D. G., Jahn, J. M., & Pollock, C. J. (2001). Initial ion equatorial pitch angle distributions from energetic netural atom images obtained by IMAGE. *Geophysical Research Letters*, 28, 1155–1158.

Perez, J. D., Zhang, X. X., Brandt, P. C., Mitchell, D. G., Jahn, J. M., & Pollock, C. J. (2004). Dynamics of ring current ions as obtained from IMAGE/HENA and IMAGE/MENA images. *Journal of Geophysical Research*, 109, A05208. https://doi.org/10.1029/2003JA010164

Pollock, C. J., Isaksson, A., Jahn, J.-M., Søraas, F., & Sørbø, M. (2009). Remote global-scale observations of intense low-altitude ENA emissions during the Halloween geomagnetic storm of 2003. *Geophysical Research Letters*, 36, L19101. https://doi.org/10.1029/2009GL038853.1987

Rairden, R. L., Frank, L. A., & Craven, J. D. (1986). Geocoronal imaging with Dynamics Explorer. *Journal of Geophysical Research*, 91, 13,613–13,630. https://doi.org/10.1029/JA091iA12p13613

Roelof, E. C. (1987). Energetic neutral atom image of a storm-time ring current. *Geophysical Research Letters*, 14, 652–655.

Roelof, E. C., & Skinner, A. J. (2000). Extraction of ion distributions from magnetospheric ENA and EUV images. *Space Science Reviews*, 91, 437–459.

Roelof, E. C., Mitchell, D. G., & Williams, D. J. (1985). Energetic neutral atoms (E ∼ 50 keV) from the ring current: IMP 7/8 and ISEE 1. *Journal of Geophysical Research*, 90, 10,991–11,008. https://doi.org/10.1029/JA090iA11p10991

Scime, E. E., Keesee, A. M., Jahn, J., Kline, J. L., Pollock, C. J., & Thomsen, M. (2002). Remote ion temperature measurements of Earth's magnetosphere: Medium energy neutral atom (MENA) images. *Geophysical Research Letters*, 29(10), 1438. https://doi.org/10.1029/2001GL013994

Sckopke, N. (1966). A general relation between the energy of trapped particles and the disturbance field near the Earth. *Journal of Geophysical Research*, 71, 3125–3130. https://doi.org/10.1029/JZ071i013p03125

Shue, J.-H., Chao, J. K., Fu, H. C., Russell, C. T., Song, P., Khurana, K. K., & Singer, H. J. (1997). A new functional form to study the solar wind control of the magnetopause size and shape. *Journal of Geophysical Research*, 102, 9497–9512. https://doi.org/10.1029/97JA00196

Singer, S. F. (1957). A new model of magnetic storms and aurorae. *Transactions, American Geophysical Union*, 38, 175–190. https://doi.org/10.1029/TR038i002p00175

Singer, S. F. (1960). Structure of the Earth's exosphere. *Journal of Geophysical Research*, 65(9), 2577. https://doi.org/10.1029/JZ065i009p02577

Spence, H. E., & Kivelson, M. G. (1993). Contributions of the low-latitude boundary layer to the finite width magnetotail convection model. *Journal of Geophysical Research*, *98*, 15,487–15,496.

Stuart, G. W. (1959). Satellite-measured radiation. *Physical Review Letters*, *2*, 417. https://doi.org/10.1103/PhysRevLett.2.417

Sugiura, M., & Kamei, T. (1991). Equatorial DST index 1957 to 1986. In A. Berthelier, & M. Menvielle (Eds.), *IAGA Bull. 40*. Saint Maur France: International Service for Geomagnetic Indices Publication Office.

Terasawa, T., Fujimoto, M., Mukai, T., Shinohara, I., Saito, Y., Yamamoto, T., et al. (1997). Solar wind control of density and temperature in the near-Earth plasma sheet: WIND/GEOTAIL collaboration. *Geophysical Research Letters*, *24*, 935–938. https://doi.org/10.1029/96GL04018

Thomsen, M. F., Borovsky, J. E., Skoug, R. M., & Smith, C. W. (2003). Delivery of cold, dense plasma sheet material into the near-Earth region. *Journal of Geophysical Research*, *108*(A4), 1151. https://doi.org/10.1029/2002JA009544

Tsurutani, B. T., Gonzalez, W. D., Gonzalez, A. L. C., Tang, F., Arballo, J. K., & Okada, M. (1995). Interplanetary origin of geomagnetic activity in the declining phase of the solar cycle. *Journal of Geophysical Research*, *100*, 21,717–21,733. https://doi.org/10.1029/95JA01476

Tsurutani, B. T., Gonzalez, W. D., Gonzalez, A. L. C., Guarnieri, F. L., Gopalswamy, N., Grande, M., et al. (2006). Corotating solar wind streams and recurrent geomagnetic activity: A review. *Journal of Geophysical Research*, *111*, A07S01. https://doi.org/10.1029/2005JA011273

Tsurutani, B. T., Smith, E. J., Gonzalez, W. D., Tang, F., & Akasofu, S. I. (1988). Origin of interplanetary southward magnetic fields responsible for major magnetic storms near solar maximum (1978–1979). *Journal of Geophysical Research*, *93*, 8519–8531. https://doi.org/10.1029/JA093iA08p08519

Tsyganenko, N. A., & Mukai, T. (2003). Tail plasma sheet models derived from Geotail particle data. *Journal of Geophysical Research*, *108*(A3), 1136. https://doi.org/10.1029/2002JA009707

Tsyganenko, N. A., & Sitnov, M. I. (2005). Modeling the dynamics of the inner magnetosphere during strong geomagnetic storms. *Journal of Geophysical Research*, *110*, A03208. https://doi.org/10.1029/2004JA010798

Valek, P., Brandt, P. C., Buzulukova, N., Fok, M.-C., Goldstein, J., McComas, D. J., et al. (2010). Evolution of low altitude and ring current ENA emissions from a moderate magnetospheric storm: Continuous and simultaneous TWINS observations. *Journal of Geophysical Research*, *115*, A11209. https://doi.org/10.1029/2010JA015429

Valek, P. W., Delmonico, E. B., Goldstein, J., McComas, D. J., & Perez, J. D. (2018). Extended energy, composition separated ENA observations of the St. Patricks day storm. *Journal of Geophysical Research*, *123*. https://doi.org/10.1002/2017JA024997

Valek, P. W., Goldstein, J., Jahn, J.-M., McComas, D. J., & Spence, H. E. (2015). First joint in situ and global observations of the medium-energy oxygen and hydrogen in the inner magnetosphere. *Journal of Geophysical Research: Space Physics*, *120*, 7615–7628. https://doi.org/10.1002/2015JA021151

Valek, P., Goldstein, J., McComas, D. J., Fok, M., & Mitchell, D. G. (2014). Large magnetic storms as viewed by TWINS: A study of the differences in the medium energy ENA composition. *Journal of Geophysical Research: Space Physics*, *119*, 2819–2835. https://doi.org/10.1002/2014JA019782

Valek, P. W., Goldstein, J., McComas, D. J., Iiie, R., Buzulukova, N., Fok, M.-C., & Perez, J. D. (2013). Oxygen-hydrogen differentiated observations from TWINS: The 22 July 2009 storm. *Journal of Geophysical Research: Space Physics*, *118*, 3377–3393. https://doi.org/10.1002/jgra.50204

Vallat, C., Dandouras, I., Brandt, P. C., & Mitchell, D. G. (2004). First comparison between ring current measurements by Cluster/CIS and IMAGE/HENA. *Journal of Geophysical Research*, *109*, A04213. https://doi.org/10.1029/2003JA010224

Wang, C.-P., Lyons, L. R., Weygand, J. M., Nagai, T., & McEntire, R. W. (2006). Equatorial distributions of the plasma sheet ions, their electric and magnetic drifts, and magnetic fields under different interplanetary magnetic field bz conditions. *Journal of Geophysical Research*, *111*, A04215. https://doi.org/10.1029/2005JA011545

Wanliss, J. A., & Showalter, K. M. (2006). High-resolution global storm index: Dst versus SYM-H. *Journal of Geophysical Research*, *111*, A02202. https://doi.org/10.1029/2005JA011034

Webb, D. F., & Howard, R. A. (1994). The solar cycle variation of coronal mass ejections and the solar wind mass flux. *Journal of Geophysical Research*, *99*, 4201–4220. https://doi.org/10.1029/93JA02742

Weimer, D. R. (2001). An improved model of ionospheric electric potentials including substorm perturbations and application to the geospace environment modeling November 24, 1996, event. *Journal of Geophysical Research*, *106*, 407–416. https://doi.org/10.1029/2000JA000604

Westlake, J. H., Mitchell, D. G., Brandt, P. C.-s., Andrews, B. G., & Clark, G. (2016). The Low-Energy Neutral Imager (LENI). *Journal of Geophysical Research: Space Physics*, *121*, 8228–8236. https://doi.org/10.1002/2016JA022547

Wood, K., Perez, J. D., Goldstein, J., McComas, D. J., & Valek, P. W. (2015). Field aligned currents derived from pressure profiles obtained from TWINS ENA images for geomagnetic storms that occurred On 01 June 2013 and 17 March 2015, sM51D-2516.

Yokoyama, N., & Kamide, Y. (1997). Statistical nature of geomagnetic storms. *Journal of Geophysical Research*, *102*, 14,215–14,222. https://doi.org/10.1029/97JA00903

Yonezawa, T. (1966). Theory of the formation of the ionosphere. *Space Science Reviews*, *5*, 3–56. https://doi.org/10.1007/BF00179214

Zhang, X. X., Perez, J. D., Chen, T., Wang, C., Brandt, P. C., Mitchell, D. G., & Wang, Y. L. (2005). Proton temperatures in the ring current from ENA images and in situ measurements. *Geophysical Research Letters*, *32*, L16101. https://doi.org/10.1029/2005GL023481

Zoennchen, J. H., Bailey, J. J., Nass, U., Gruntman, M., Fahr, H. J., & Goldstein, J. (2011). The TWINS exospheric neutral H-density distribution under solar minimum conditions. *Annales Geophysicae*, *29*, 2211. https://doi.org/10.5194/angeo-29-2211-2011

Zoennchen, J. H., Nass, U., & Fahr, H. J. (2013). Exospheric hydrogen density distributions for equinox and summer solstice observed with TWINS1/2 during solar minimum. *Annales Geophysicae*, *31*, 513. https://doi.org/10.5194/angeo-31-513-2013

Zoennchen, J. H., Nass, U., & Fahr, H. J. (2015). Terrestrial exospheric hydrogen density distributions under solar minimum and solar maximum conditions observed by the TWINS stereo mission. *Annales Geophysicae*, *33*, 413. https://doi.org/10.5194/angeo-33-413-2015

Zoennchen, J. H., Nass, U., Fahr, H. J., & Goldstein, J. (2017). The response of the H-geocorona between 3 to 8 Re to geomagnetic disturbances sutdied by TWINS stereo Lyman-alpha data. *Annales Geophysicae*, *35*, 171. https://doi.org/10.5194/angeo-35-171-2017

Zoennchen, J. H., Nass, U., Lay, G., & Fahr, H. J. (2010). 3D-geocoronal hydrogen density derived from TWINS Ly-alpha-data. *Annales Geophysicae*, *28*, 1221. https://doi.org/10.5194/angeo-28-1221-2010